ABSTRACT

Embayments in Explosive, Silicic Eruptions: A Textural, Numerical, and Experimental Assessment

Anna C. Ruefer, M.S.

Mentor: Kenneth S. Befus, Ph.D.

I explore the occurrence and formation of embayments in quartz using textural, experimental, and numerical techniques. Embayments are pockets of melt partially trapped inside of volcanic crystals. During eruption these pockets of melt quench to glass. The concentration of water within embayment glass is the foundation for a powerful new technique in volcanology that is thought to record how quickly the magma ascended during an eruption. My goal was to determine how accurately embayments record changes in the magma during ascent. Using a high-pressure, high-temperature system, I performed decompression experiments on natural and synthetic embayments to test their ability to record magmatic conditions. Experimental work is thus far unsuccessful but highlights best practices for researchers going forward. My work on rhyolitic eruptions shows that embayments are common across eruptions. The range in embayment shapes and textures preserves a record of three separate timescales: diffusion speedometry, emptying, and faceting.

Embayments in Explosive, Silicic Eruptions: A Textural, Numerical, and Experimental Assessment

by

Anna Ruefer, B.S.

A Thesis

Approved by the Department of Geosciences

Joe Yelderman, Ph.D., Chairperson

Submitted to the Graduate Faculty of
Baylor University in Partial Fulfillment of the
Requirements for the Degree
of

Master of Science

Approved by the Thesis Committee

Kenneth Befus, Ph.D., Chairperson

Steven Forman, Ph.D.

Peter James, Ph.D.

Christie Sayes, Ph.D.

Accepted by the Graduate School

August 2021

J. Larry Lyon, Ph.D., Dean

Page bearing signatures is kept on file in the Graduate School.

TABLE OF CONTENTS

LIST OF FIGURES

LIST OF TABLES

ACKNOWLEDGMENTS

Dr. Kenny Befus – Thank you for your constant mentorship, for cheering me on, pulling me out of rabbit holes, equipping me with confidence, and modeling what it looks like to do excellent science without compromising a healthy research community. I owe so much to your leadership and guidance.

Dr. Ben Andrews – Thank you for taking the lead on collecting CL imagery for this research. Your insights and engagement have improved the manuscript significantly.

Dr. James Thompson – Thank you for contributing your coding and numerical expertise to this research. You have been a constant source of support, encouragement, positivity, and knowledge. I'm going to miss tea-time.

Dr. Chelsea Allison – Thanks for always being excited to geek out over embayments with me. Your enthusiasm, creativity, and mentorship helped to push me through the finish line of this research.

Dr. Roy Bassoo – Thank you for being an excellent officemate and even better model of determination, focus, and hard work. Your passion for science and willingness to help others spurred me on every day.

Dr. Peter James – Thank you for your mentorship and support during my time at Baylor. Your patience and willingness to engage with me both on my thesis as a committee member, in class, and other research, humoring the bad puns all throughout, enabled me to grow into a much stronger scientist.

Dr. Steve Forman – Thank you for being a member of my thesis committee and a constant supporter over the course of my Master's. Your encouragement and teaching equipped me with the confidence to pursue my Ph.D.

Dr. Christie Sayes – Thank you for serving on my thesis committee and for being a source of creativity, positivity, and curiosity.

Nick Meszaros – Thank you for sending material from the Bandelier Tuff. It was one of my favorite samples to work with from the entire study.

Dr. Madison Myers – Thank you for providing samples of the Oruanui and Huckleberry Ridge Tuff and for your collaborative support since my undergraduate research continuing through graduate school.

Dr. Steve Self – Thank you for providing samples of Toba Tuff welded ignimbrite.

Dr. Joe Dufek – Thank you for sending samples of the Kos Plateau Tuff.

Dr. Giovani Sosa – Thank you for sending samples of the La Primavera Giant Pumice horizon. It was a pleasure getting to know you as our group suffered through doubly polishing some very challenging quartz crystals.

CHAPTER ONE

Introduction

Eruptive style largely dictates the extent and nature of hazards imposed by a volcanic event. Explosive eruptions pose the greatest risk to life and infrastructure. They also are generated by rapid magmatic ascent, the rate of melt transport from shallow, crustal storage to the surface (Cassidy et al., 2018). During ascent, magma decompresses, lowering volatile solubility and driving exsolution via diffusion (Hurwitz and Navon, 1994; Gonnermann and Manga, 2007; Coumans et al., 2020). In high viscosity, silicic melts this degassing response is outpaced by rapid ascent, preventing equilibrium bubble nucleation and growth (Gardner et al, 2000; Castro and Gardner, 2008). This produces an increasingly volatile supersaturated magma that results in powerful explosivity (Rutherford, 2008; Mangan and Sisson, 2000). The role of magmatic ascent is thus intrinsic to understanding the timing of volcanism and informing emergency responses following precursor activity (Castro and Dingwell, 2009; Myers et al., 2018).

The rate, mechanisms, and evolution of magma transport cannot be directly observed, instead requiring the study of post-eruptive materials. Previous studies have used indirect methods, including conduit modeling (Wilson et al., 1980; Mastin, 2002), bubble and microlite nucleation (Toramaru, 2006; Toramaru et al., 2008; Befus and Andrews, 2018), groundmass crystallization (Cashman, 2004, 1992; Nakada and Motomura, 1999), and hydrous mineral breakdown (Rutherford and Hill, 1993; Browne and Gardner, 2006). Melt embayments, the open, volatile-exchanging relative of melt

inclusions (Figure 1.1), provide another method for ascent rate estimation (Anderson, 1991; Liu et al., 2007; Humphreys et al., 2008).

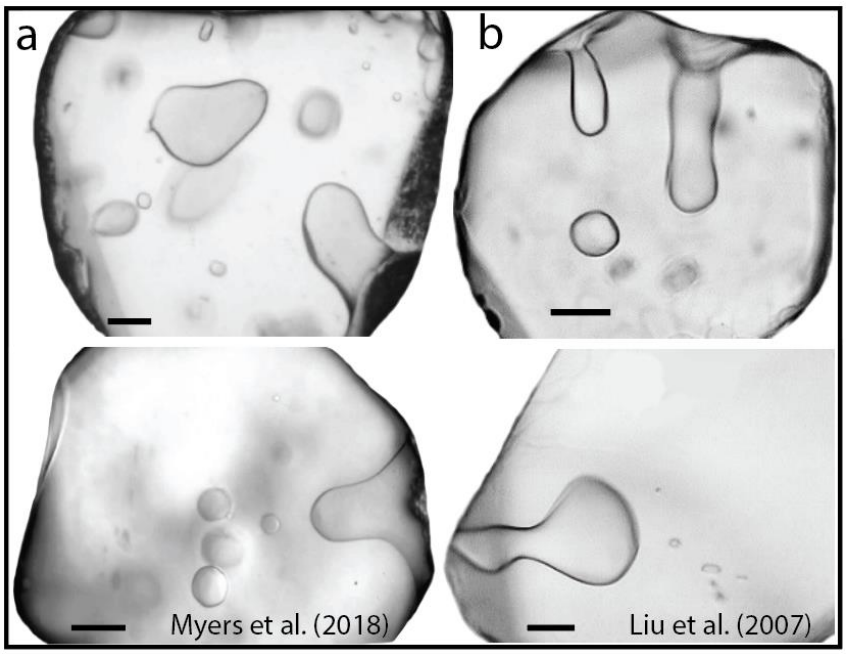

Figure 1.1. a) Photomicrographs of Bishop Tuff embayments from Myers et al. (2018) and b) Oruanui embayments from Liu et al. (2007). Black lines are 100 μm scale bars.

Embayments, also called reentrants or hourglass inclusions, were observed and described in literature nearly 100 years ago (Lemmlein, 1930). They have since been documented in various systems with increasing frequency in the past few decades (Busby and Barker, 1966; Roedder et al., 1979; Donaldson and Henderson, 1988; Harris and Anderson, 1984; Frezotti 2000; Lowenstern 1995, 2003; Anderson, 1991). Embayments are common features in crystals formed from most magma compositions and can record rapid ascent over short timescales (Figure 2a), an advantage over previous techniques for explosive systems (Myers et al., 2018). The mechanism responsible for their formation remains debated. Embayment formation likely occurs either via rapid growth (e.g.,

Roedder, 1979; Loewen et al., 2017; Barbee et al., 2020) or dissolution following bubble nucleation on the crystal surface (Busby and Barker, 1966; Donaldson and Henderson, 1988; Harris and Anderson, 1984; Befus and Manga, 2019). These melt pockets have been studied in plagioclase (Humphreys et al., 2008) and quartz hosts (Myers et al. 2016, 2018, 2021; Liu et al., 2007) for Plinian to sub-Plinian, silicic eruptions, and olivine in Hawaiian to Strombolian, basaltic systems (Lloyd et al., 2014; Ferguson et al., 2016; Moussallam et al., 2019; Newcombe et al., 2020). Embayments are typically clear, glassy, and free of microlites and bubbles, but bubbles have been described in some studies, often present at embayment outlets (Anderson, 1991; Liu et al., 2007; Myers et al., 2016, 2018). The occurrence of hollow embayments in quartz phenocrysts from the Yellowstone Lava Creek Tuff suggests that extreme cases of vesiculation within the pockets is possible, implicating residence in a highly volatile-saturated, bubbly magma chamber prior to eruption (Befus and Manga, 2019).

The melt in the embayments experience decompression during eruptive magmatic ascent. The diffusion of volatiles from the interior to the exterior of an embayment in response to decompression is a time-dependent process and could theoretically provide a quantitative record of magmatic ascent rate. The host crystals rapidly cool upon eruption, thereby quenching the melt to glass and preserving volatile gradients in embayment glass (Figure 1.2). This unique potential for recording magmatic and eruptive conditions was first recognized by Anderson (1991). Additionally, this study first proposed a model for melt emptying through embayments with small, constricted necks (hourglass inclusions) and implications for ascent.

Under Anderson's tutelage, Liu et al. (2007) provided a foundational, theoretical basis for their use as ascent speedometers. This application has accelerated rapidly in the past 10 years, growing towards an established technique for ascent rate estimation in both mafic and silicic systems (Liu et al., 2007; Humphreys et al., 2008; Myers et al., 2016, 2018, 2021; Lloyd et al., 2014; Ferguson et al., 2016; Moussallam et al., 2019; Newcombe et al., 2020).

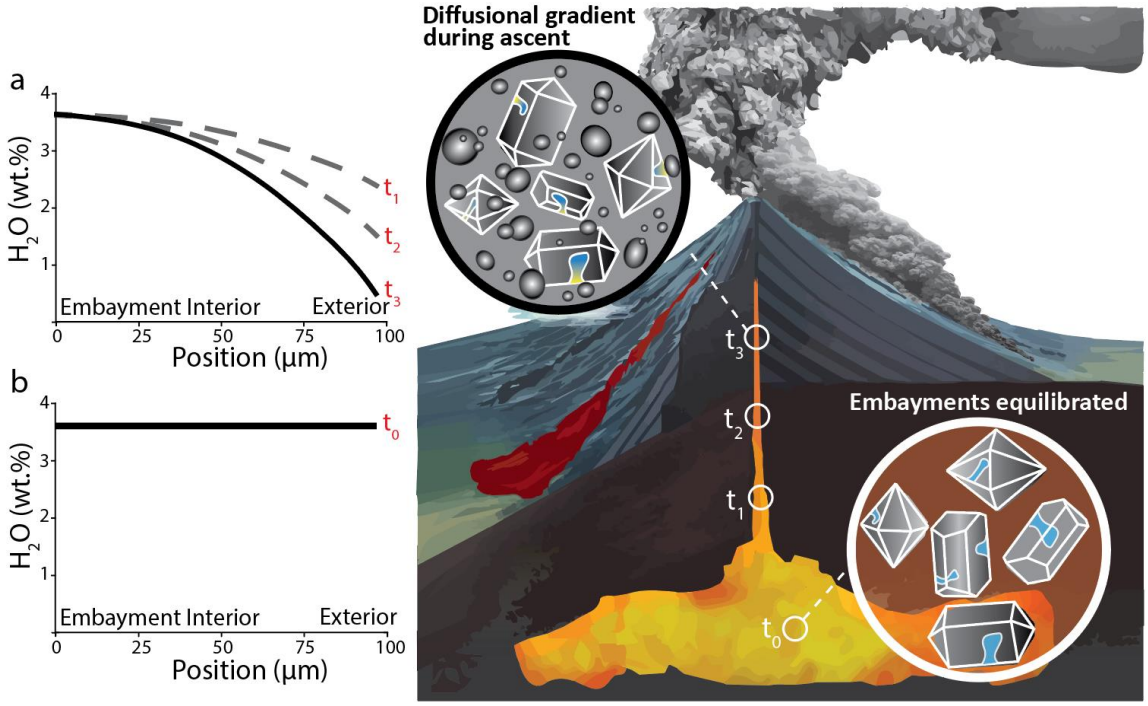

Figure 1.2. Schematic illustrating initial embayment equilibration in a shallow, pre-eruptive magma chamber at t_o and b) expected H_2O profile; a) as magma ascends (t_{1-3}), water begins to diffuse out of the embayment, producing corresponding diffusion profiles.

Research Problem

In total, embayment diffusion geospeedometry has only been applied to 75 embayments across 9 studies for both mafic and silicic systems (Ferguson et al., 2016; Lloyd et al., 2014; Myers et al., 2016, 2018; 2021; Humphreys et al., 2008; Liu et al., 2007; Moussallam et al., 2019; Newcombe et al., 2020). Despite increased application, this method remains limited by small datasets and unconstrained complexities inherent to the technique. For the Plinian, Oruanui supereruption, decompression rates calculated by Liu et al. (2007) ranged between 0.001-0.007 MPa s^{-1} (equivalent to ~0.03-0.21 m s^{-1}) using 8 embayments. Myers et al. (2018) estimated 0.003-0.11 MPa s^{-1} (0.09-3.3 m s^{-1}) using an additional 9 measurements from the same eruption. This range suggests ascent timescales between tens of minutes and several hours for melt from the Oruanui eruption. Estimates from Mount St. Helens ranging from 0.9-1.6 MPa s^{-1} (27-48 m s^{-1}), suggesting timescales as few as 3 minutes for melt to ascend from a 5-km-deep magma reservoir to the surface (Humphreys et al., 2008). Thus, there are order of magnitude variations within single events, as well as even larger variations when comparisons are made between separate eruptions (Figure 1.3).

Myers et al. (2021) analyzed the greatest number of embayments in a single study to date, with 16 embayments in both plagioclase and pyroxene hosts from the Santorini Volcano Late-Bronze Age eruption. Of these, 5 diffusion profiles were flat, and only the remaining 11 could be used for ascent rate estimates. This means over 30% of embayments selected, prepared, and analyzed for speedometry were re-equilibrated and did not record decompression. Ascent rates from the remaining 11 embayments ranged between 0.008 to 0.25 MPa s^{-1} (0.24-7.5 m s^{-1}).

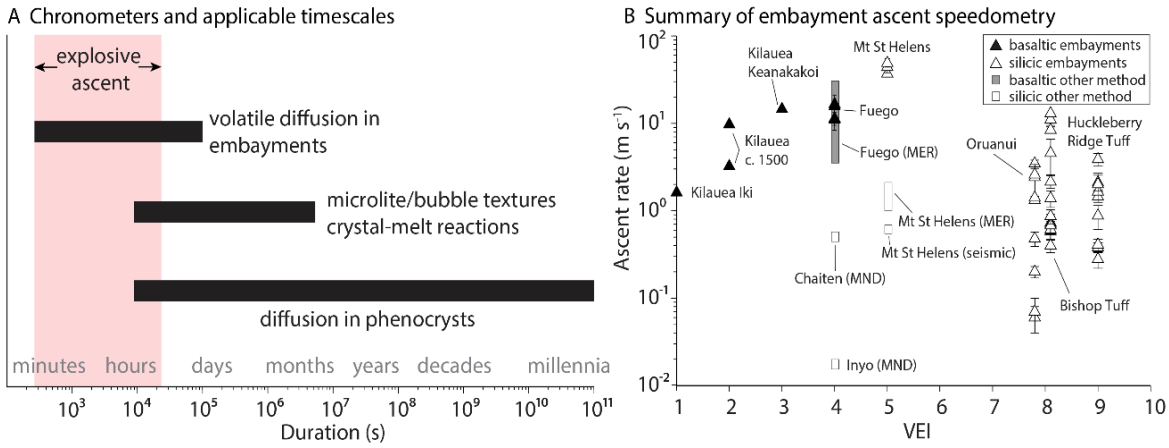

Figure 1.3. a) Overview of the applicable timescales for previously used magmatic ascent chronometers compared to embayments; b) ascent estimates for different eruptions reported using embayments in existing studies.

The inconsistency in diffusion profiles and ascent estimates may be representative of real eruptive variability. Alternatively, the inconsistencies may be produced by poorly understood complexities within embayments, including geometry, bubble textures, and viscous shielding. Indeed, the variable geometry and orientation of natural embayments encumbers sample preparation. The difficulty in sample preparation is the primary reason why earlier datasets relied on such limited numbers of embayments. The effect of embayment diameter on diffusion is predicted to be negligible, assuming it is small with respect to length (Liu et al., 2007). However, as embayment neck diameter decreases and diffusion duration increases, relative error in modeled diffusion timescales increases (deGraffenreid and Shea, 2021). Thus, there may be an ideal range of embayment diameter and lengths capable of accurately preserving concentration gradients. But how does embayment geometry introduce inaccuracy to diffusion models? It may be that greater pressure is imposed on embayment melt by geometry and viscous shielding that prevents the embayment interior from feeling the actual pressure in the system (Liu et al.,

2007). This shielding process may also reconcile the relative lack of bubbles within some embayments despite the surrounding matrix being highly vesiculated (Anderson, 2006).

The main analytical approaches supporting the research herein requires understanding water-melt solubility and diffusion theory. Water content in rhyolite glass can be analyzed using Fourier Transform Infrared Spectrometry (FTIR). This technique is the most common approach used to measure water contents in volcanic glass. To prepare a sample for FTIR analysis, the embayment-hosting crystal is ground down until embayment glass is exposed and polished to a mirror-like finish. After flipping the crystal, this process is repeated on the opposite side. The final sample is a thin wafer of crystal and doubly exposed embayment glass. The embayment glass is analyzed for water content along a transect from the melt pocket interior to exterior using a FTIR with ~20 µm spatial resolution. FTIR operates by passing infrared light through glass. Water occurs as two species: hydroxyl (OH^-) and molecular water (H_2O_m). The species absorb the infrared light which produces characteristic absorption peaks at different wavenumbers (Figure 1.4) (Stolper, 1982).

Absorbance peak height can be converted to absolute water concentration using the Beer-Lambert Law (Newman, 1986; Zhang, 1999):

(1) $$c_i = \frac{M_i A}{\rho d \varepsilon}$$

Where c_i is absolute water concentration, M_i is molar weight (g mol^{-1}), A is absorbance peak height, ρ is glass density (g L^{-1}), d is sample thickness (cm), and ε is the molar absorption coefficient determined for water in rhyolitic glass (Withers and Behrens, 1999; Newman et al., 1986; Ohlhorst et al., 2001).

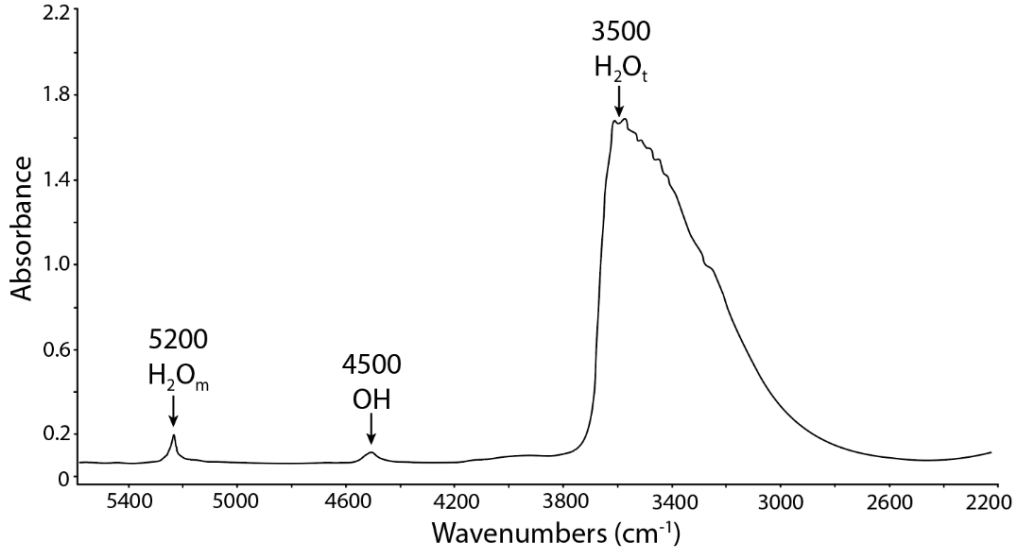

Figure 1.4. Absorbance spectra from rhyolite glass, showing characteristic peaks associated with molecular water (H_2O_m), hydroxyl (OH^-), and total water (H_2O_t).

All measured water concentration profiles across embayments can be compared to predictions produced by a numerical, finite-element diffusion model using a MATLAB script. In this model, the approach for diffusion of water in rhyolitic melts is described in Coumans et al. (2020). In one-dimension, the diffusion equation takes the basic form of Fick's second law:

$$\frac{\delta C}{\delta t} = D\frac{\delta^2 C}{\delta x^2} \quad (2)$$

Where *D* is diffusivity, *C* is concentration, *t* is time, and *x* is distance (Zhang, 2010). Importantly, the rate at which diffusive equilibrium is established in silicate melt relies upon the diffusivity of water and the concentration gradient. Diffusivity of water is then dependent on temperature, pressure, water concentration, and composition (Coumans et al., 2020; Zhang, 2010). Below 3 wt. %, H_2O diffusivity is proportional to H_2O concentration in the melt (Ni and Zhang, 2008; Zhang et al., 2007), resulting in a linear increase in diffusivity with respect to water concentration, with an exponential increase at higher concentrations (Nowak and Behrens, 1997). Furthermore, diffusivity of water

increases with increasing temperature (Zhang, 2010). Previous workers developed separate equations for water diffusivity at low- and high-water concentrations (Ni and Zhang, 2008; Zhang 2007). In an updated form, water diffusivity can be described by a piecewise functional form which simultaneously accounts for the kinetics of water speciation and the change from linear to exponential concentration dependence at low- to high-water concentration as follows (Coumans et al., 2020):

(3) $$lnD_{H_2O} = \begin{cases} lnC_{H_2O} + a_1 + a_2\frac{1000}{t} : C_{H_2O_t} \leq C_{H_2O_t}^{Brk} & (linear) \\ a_3 C_{H_2O_t} + a_4 + (a_5 C_{H_2O_t} + a_6)\frac{1000}{T} : C_{H_2O_t} > C_{H_2O_t}^{Brk} & (exponential) \end{cases}$$

Where $a_1 \ldots a_6$ are empirical coefficients, $C_{H_2O_t}^{Brk}$ is water concentration when the function shifts from linear to exponential. This can be solved numerically using MATLAB. The timing of this transport can thus be modeled forward numerically to predict the concentration gradient at an appointed temperature, pressure, and ascent rate.

To demonstrate the concept, a 2-D diffusion code is applied to embayments within a single crystal from the Bandelier Tuff to illustrate the utility of this approach for embayment speedometry (Figure 1.5). This code employs an updated 2-D approach which accounts for embayment geometry (Perron et al., 2008, 2009; Richardson 2018). An initial condition of 3 wt.% H_2O and fixed external melt value of 1 wt.% H_2O is assumed. Diffusion over the course of 0.5, 2, and 5 hours is modeled and compared to the retrieved profile. Diffusion profiles from two embayments prepared here do not record diffusion, suggesting ascent in <0.5 hours, which equates to a rapid ascent rate of 0.11 MPa s^{-1}, assuming storage depth of 200 ± 50 MPa (Boro et al., 2021).

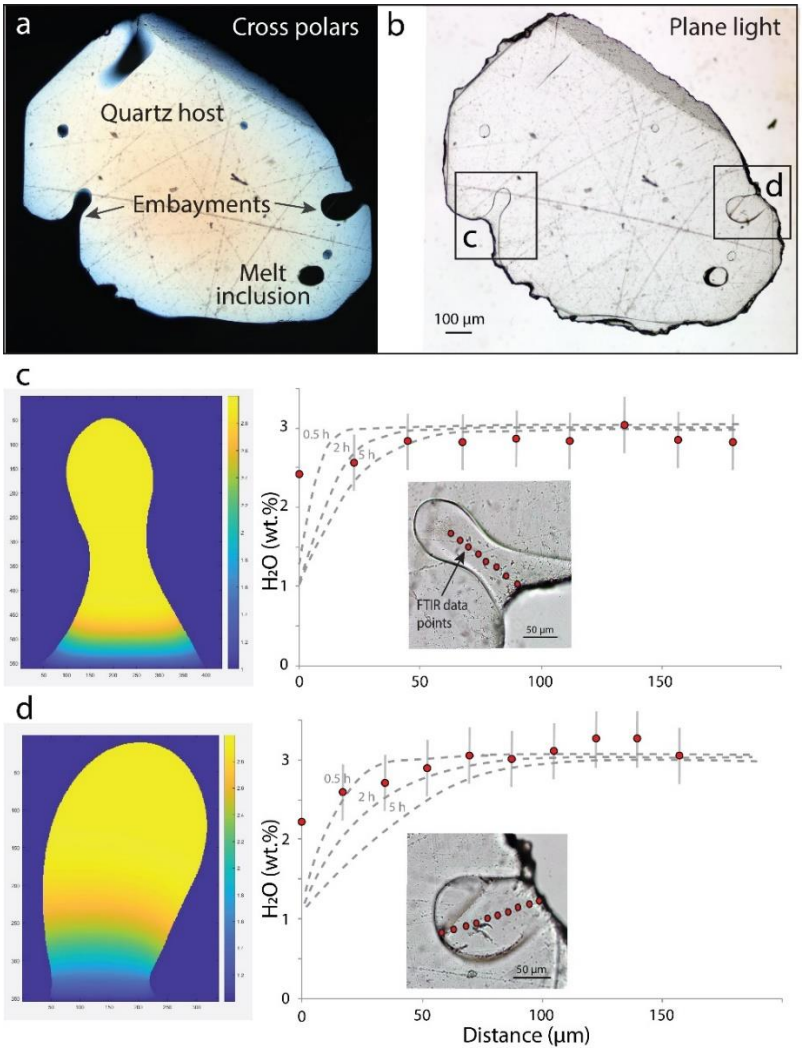

Figure 1.5. a) Photomicrograph in XPL showing crystal host, embayments, and melt inclusions; b) photomicrograph in PPL highlighting embayments analyzed for speedometry; c-d) water maps generated by diffusion code and profiles at three ascent rates (gray dashed lines) compared to actual FTIR data (red dots).

Although embayments are increasing in popularity, much remains unknown about their occurrence. The discrepancies in reported ascent estimates further highlight the need for a robust, textural and observational assessment of embayments across multiple systems. Additionally, an experimental verification of embayment speedometry is necessary. Together, these approaches will establish a better foundation for understanding embayment formation, occurrence, and morphology for the purpose of ascent rate

reconstruction. In this work, I combine these two approaches. First, I conduct a survey of quartz-hosted embayments in 10 rhyolitic, large-volume, explosive eruptions. I describe the filling characteristics, morphology, and occurrence of embayments in each eruption. To understand the mechanism for embayment formation (e.g., dissolution or growth), I also include a suite of embayments analyzed by cathodoluminescence. A numerical model for melt loss from embayments during magmatic ascent explores the effect of viscous shielding.

I also conduct a series of experiments using both natural and synthetic embayments in rhyolitic systems to explore the reliability of embayment geospeedometry. Some experiments are subjected to various decompression pathways to assess a wide range of eruptive ascent rates. Following decompression, I measure the resulting H_2O diffusion profiles preserved in experimental embayments. Ascent estimates retrieved from concentration gradients in experimentally decompressed embayments are compared to diffusion models using the known decompression rates. Unfortunately, the experimental approach proved to be very challenging. Through various unsuccessful attempts, I have learned much about the inherent pitfalls in this research. Particularly, a persistent problem is bubble nucleation where bubble-free, dense glass is required for success. The attempts made in this research so far, and the associated challenges, illustrates the need and opportunity for future work.

CHAPTER TWO

Anthology of Quartz-hosted Embayment Textures

Introduction

Volcanic rocks preserve textures that reflect the dynamic magmatic and volcanic processes which lead to their formation, eruption, and preservation. The textures can be interpreted to infer processes in the subsurface that are not directly observable, including pre-eruptive magmatic storage, magmatic ascent, and fragmentation (e.g., Rutherford, 2008; Toramaru et al, 2006; 2008; Gardner et al., 2017). Some textures can be used as geospeedometers because they preserve information about the rates and timescales over which processes occur (e.g., Cashman, 1992; Pamukcu et al., 2015; Hajimirza et al., 2021).

Glass-filled pockets in volcanic phenocrysts, called embayments or reentrants, have been exploited as a compositional, petrologic record of magmatic ascent. Ascent rate exerts a primary control over eruptive style and explosivity (Cassidy et al., 2018; Castro and Dingwell, 2009; Castro and Gardner, 2008). For this reason, embayments have been increasingly applied as a geospeedometer for silicic and mafic systems (e.g., Myers et al., 2016; 2018; 2021; Liu et al., 2007; Lloyd et al. 2014; Humphreys et al., 2008; Ferguson et al., 2016; Moussallam et al., 2019; Newcombe et al, 2020). Embayments are parcels of melt which never become fully entrapped by the crystal host. The crystalline host shields the partially enclosed melt, presumably suppressing

vesiculation and microlite nucleation. Upon eruption and quenching the embayment is preserved as a channel of glass.

During ascent, shielded embayment melt experiences diffusion-limited equilibration of volatiles with the decompressing external magma. This diffusion-limited equilibration produces volatile gradients that can be used to recover magma ascent rates with numerical modeling (e.g., Liu et al., 2007; Myers et al., 2016; 2018; 2021). Successful modeling requires dense, glassy embayments, unmarred by bubbles or microlites. Simple shaped forms are also required (deGraffenreid and Shea, 2021). These requirements for geospeedometry may have resulted in a presumptive and disproportionate overrepresentation of the description of bubble-free embayments in the literature. Embayments have been shown to be complex and multi-phased (e.g., Anderson, 1991; Liu et al., 2007; Cashman and Rust, 2016; Rust and Cashman, 2017). They may contain microlites, internal bubbles, and bubbles which extend from the exterior melt into the embayment glass. It remains unclear how common and consistent these textural complexities are from crystal to crystal, across different volcanic systems, and within individual eruptive units. These diverse textures may contain valuable information about magmatic ascent and pre-eruptive conditions.

Here, we conduct a survey of textures present in quartz-hosted embayments from ten explosive, rhyolitic eruptions. We determine the abundance of embayments in quartz from each system. We then describe embayment morphology and bubble textures present in embayment glass. Based on these descriptions, we categorize embayment and embayment-hosted bubble morphologies and quantify the abundance of each morphology. We observe distinct variations in the number of embayment crystals across

the ten systems considered. Quartz crystals from some eruptions are nearly all embayed, whereas embayments are rare in others. Embayment morphologies are consistent within all eruptions, with simple, cylindrical forms as the dominant shape. Dense, glassy embayments without bubbles predominate, but bubble textures are also pervasive and diverse. Embayment textures contain additional information about embayment formation, magmatic storage, ascent processes and have implications for embayment geospeedometry. Specifically, we conclude that embayments are capable of recording three independent timescales, the well-known volatile diffusion speedometer, a faceting timescale, and an emptying timescale controlled by viscous shielding.

Methods

Samples

Pumice samples were acquired from the Bishop Tuff, Younger Toba Tuff, Tuff of Bluff Point, Bandelier Tuff, Oruanui Tuff, Mesa Falls Tuff, Huckleberry Ridge Tuff, the Kos Plateau Tuff, and the Giant Pumice from La Primavera caldera (Table 2.1). These explosive, rhyolitic eruptions were specifically targeted because they are quartz-bearing and their locations span a range of geographic and tectonic environments. Embayments do commonly occur in other minerals but here we restrict our analysis to quartz. A representative population of 300 to 1000 quartz crystals were handpicked from the 720 μm to 2 mm fraction of sieved pyroclastic material using a binocular microscope.

The nature of the pyroclastic source material varied by eruption because of availability. For the Tsankawi, Oruanui, Giant Pumice, and Huckleberry Ridge Tuff eruptions the quartz were picked from gently crushed air-fall pumice. Quartz were picked as loose crystals from crystal-rich air-fall deposits of the Bishop Tuff and Mesa Falls

Tuff. Pumice from unwelded ignimbrites were the source of quartz for the Tuff of Bluff Point and Kos Plateau Tuff, and for a second assessment of the Bishop Tuff to compare with fall material. Densely welded ignimbrite was the best material we could acquire for the Younger Toba Tuff. We include the Younger Toba embayments in our study; however, we treat their interpretation with caution as processes in pyroclastic density currents and the resulting ignimbrites (e.g., welding and slow cooling) likely modified the glass and bubble textures in embayments from our specific sample. Because embayments extend from the crystal surface to the interior we restricted our analysis to crystals with >50% of their surface preserved and unbroken by processes during or after emplacement. In the majority of the eruptions, unbroken crystals were common and easy to select. In the Younger Toba Tuff, Oruanui Tuff, and Bishop Tuff most quartz occurred as fragments. In these eruptions our descriptions are robust because of high counts but the relative proportion of textures may be diluted by too many crystal fragments.

Counting

The picked crystals were submerged in mineral oil, internally inspected, and separated into two groups: embayment-free and embayment-bearing. Each embayment-bearing crystal was further characterized based the morphology and degree of vesicularity of the embayment it hosts. To quantify the occurrence of the embayment classes, we established a counting scheme based on the 5 observed categories for bubble textures and embayment geometries. Most crystals contained more than 1 embayment. Some contained dozens. Within a single crystal, it is common for up to 3 textural and

morphological classes to occur simultaneously. To simplify our approach, only the first incidence of each texture or shape was counted for each individual crystal.

Table 2.1. Review of eruption parameters, including age, mineral phases, eruptive volume, and previous decompression rate estimates.

Volcano	Unit	Deposit	Mineral phases	Eruption age (Ma)	Erupted volume (km^3)	Previous decompression rate estimates (MPa s^{-1})
Valles	Upper Bandelier Tuff	Tsankawi Pumice Fall	qtz, san, pyx, mgt, ap, hbl, bt, il	1.14	250	0.0021-0.022
Taupo	Oruanui	Fall (F1-2)	plag, qtz, opx, hbl, mgt, il	0.026	430	0.001-0.11
Kos	Kos Plateau Tuff	Ignimbrite (E)	plag, san, qtz, bt, il, mgt, mon, zr, ap	0.16	60	na
Yellowstone	Huckleberry Ridge Tuff	Fall	qtz, san, plag, cpx, fay	2.1	2450	0.009-0.12
Yellowstone	Mesa Falls Tuff	Fall	qtz, san, plag, pyx, ox, zr	1.3	280	na
Yellowstone	Tuff of Bluff Point	Ignimbrite	qtz, san, plag	0.161	50	na
Long Valley	Bishop Tuff	Fall (F1-F3)	plag, san, bt, qtz	0.76	650	0.02-0.38
Long Valley	Bishop Tuff	Ignimbrite (Ig2Ea)	plag, san, bt, qtz	0.76	650	0.02-0.38
La Primavera	Giant Pumice	Lava dome	san, qtz, opx, fay, il, mgt	0.086	20	na
Toba	Younger Toba Tuff	Welded ignimbrite	qtz, san, plag, hbl, bt, opx, zr, mgt, il	0.074	2800	na

Bandelier data from Saalfeld et al., 2019; Dunbar and Hervig, 1992.
Tuff of Bluff Point data from Christiansen, 2001.
Bishop Tuff data from Hildreth and Wilson, 2007.
Giant Pumice data from Sourisseau et al., 2020.
Younger Toba Tuff data from Barbee et al., 2020.
Oruanui data from Liu et al., 2006, 2007; Myers et al., 2018; Wilson et al., 2006.
Kos Plateau Tuff data from Bachmann et al., 2007.
Huckleberry Ridge Tuff data from Myers et al., 2018.
Mesa Falls Tuff data from Rivera et al., 2016.
"na" is unavailable data.

For example, consider a single crystal with 6 embayments, 3 of which contained Texture A, 2 with Texture B, and 1 with Texture C. This crystal would count as "1" in the embayment-bearing category and "1" in each of the sub-categories: A, B, and C. We acknowledge that our approach establishes the relative abundance of embayment textures but does not quantify the absolute numbers. Multiple authors performed counts and textural analyses. To test reproducibility between the authors, subsets of crystals from the same sample were independently categorized. Results from these tests produced differences ranging up to 10%.

Cathodoluminescence (CL) Imagery

Quartz crystals from eight of the ten eruptions were selected for cathodoluminescence (CL) imagery. From each eruption, embayments of varying morphologies were selected, singly exposed, and polished. CL images were collected using the Smithsonian Institution JEOL JXA-8530FPlus HyperProbe Electron Probe

Microanalyzer (EPMA). Images were acquired with a focused 15 kV, 50 nA beam, with dwell times of 2-5 ms per pixel. The CL images were sized for nominal resolution of 0.5-1 mm pixel^{-1}, with image acquisition time ranging from 45 to 300 minutes.

Results

The crystalline form of quartz varied by eruption. Most eruptions preserve collections of multiple forms occurring together, including beta quartz bipyramids, partial bipyramids, and rounded, anhedral grains. Rounded, anhedral crystals tend to contain more embayments than euhedral bipyramids.

Embayment form varies widely in their morphology and size (Table 2.2). Morphology does not show a strong correlation with size. The prevalence of specific embayment morphologies was also determined for the eruptions. Morphologies were classified into five categories: simple, bulbous, bent, hourglass, and complex (Figure 2.1, 2.2). Simple embayments are those ideal for embayment speedometry with near-perfect cylindrical geometry and little to no tapering of the outlet. Bulbous embayments display a neck that tapers towards the outlet, extending from a rounded interior. Bent embayments exhibit a relatively simple symmetry near the outlet before a sharp 70-100^{o} shift in direction, forming a hook-like geometry. Hourglass embayments, sometimes referred to as hourglass inclusions in the literature (e.g., Lowenstern, 2003; Anderson, 1991), are characterized by a thin, threadlike outlet connected to an interior inclusion.

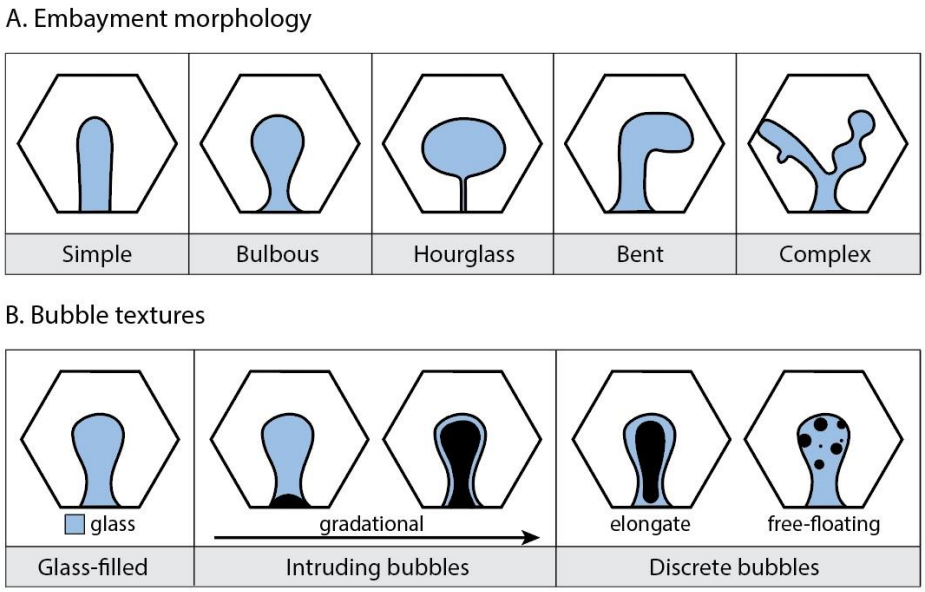

Figure 2.1. Simplified schematic of b) embayment morphologies, b) idealized bubble textures, and associated naming system.

Table 2.2. Observed bubble textural percentages.

Filling character	Bandelier Tuff	Tuff of Bluff Point	Huckleberry Ridge (F1-F3)	Giant Pumice	Bishop Tuff (Ig2Ea)	Mesa Falls Tuff	Kos Plateau Tuff	Bishop Tuff (F1-F3)	Oruanui Tuff	Younger Toba Tuff
Glassy	63	43	49	73	39	49	18	45	44	17
Intruded	15	12	39	20	31	41	29	37	48	33
Free-floating	12	11	3	2	28	3	19	13	5	22
Elongate	8	5	1	4	3	1	12	4	3	17
Decrepitated	2	29	8	0	0	7	23	2	0	11
Embayed	85	82	71	69	55	53	49	37	34	4
n	678	597	526	279	877	530	453	432	616	1764

Table 2.3. Observed morphology percentages.

Morphology	Bandelier Tuff	Tuff of Bluff Point	Huckleberry Ridge	Giant Pumice	Mesa Falls Tuff	Kos Plateau Tuff	Bishop Tuff (F1-F3)	Younger Toba Tuff
Simple	40	45	51	39	37	43	50	68
Bulbous	25	25	27	30	37	35	26	23
Hourglass	4	3	2	2	4	2	1	5
Bent	7	7	4	8	8	4	4	0
Complex	24	20	16	21	14	16	18	5
n	302	720	228	425	497	453	106	22

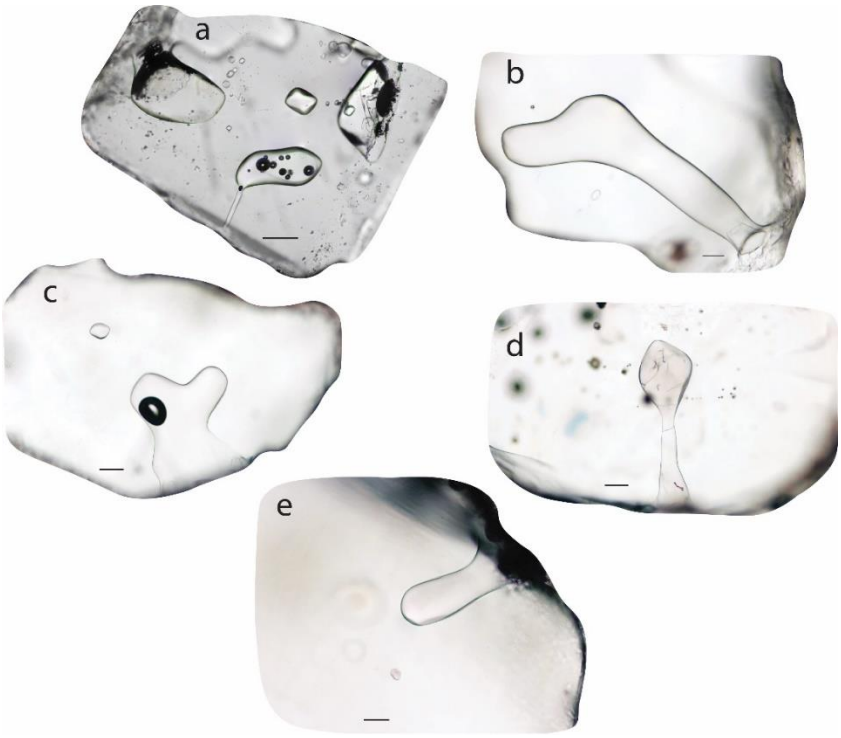

Figure 2.2. Photomicrographs of embayment morphology classifications; a) hourglass inclusion from the Bandelier Tuff (with discrete bubbles); b) a bent embayment within the Kos Plateau Tuff; c) complex embayment from the Kos Plateau Tuff (with a discrete bubble); d) bulbous embayment in the Huckleberry Ridge Tuff; e) simple embayment from the Mesa Falls Tuff. Scale bar in each panel is 100 μm.

Complex embayments are those which display any additional morphology. This category includes branching and crosscutting embayments. Embayment morphologies are notably similar across all eruptions in this study, with counts varying by no more than 14% (Table 2.2). Simple embayments are the most common (37-51%), followed by bulbous (25-30%), complex (14-24%), bent (4-8%), and hourglass (1-4%).

Select embayment-bearing quartz crystals were selected for synchrotron X-ray microtomography (μXRT) at the Lawrence Berkley National Laboratory Advanced Light Source. 3-D geovisualization and measurements with micron-scale resolution confirm petrographic observations of embayment filling textures (Figure 2.3). Bubbles occur in

embayments. Individual crystals can preserve embayments with disparate bubble textures.

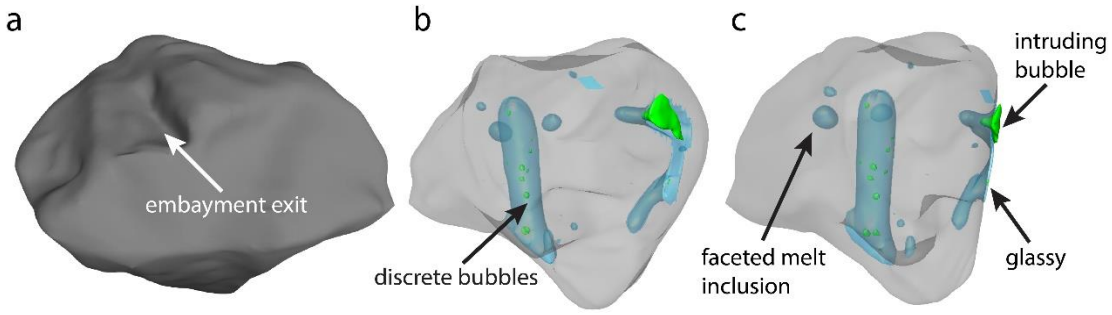

Figure 2.3. 3-D visualization of a quartz crystal from the Bishop Tuff showing the a) exterior crystal form and pockmarked texture at embayment exits; b-c) internal views of the same crystal rotated, showing the filling character of embayments. Glass in blue, quartz in gray, and glass in green.

Cross-cutting or deflecting relationships preserved by bands of variable contrast visible in CL images lend insight into the mechanism controlling embayment formation (Figure 2.4). CL images of embayments in quartz were inspected carefully and categorized as having formed via growth, dissolution, or undetermined. Growth embayments were recognized by zone adaptations, deflected CL bands, and inward tapering of bands. Embayments formed via dissolution exhibited cross-cutting to dissected bands and smooth zone boundaries. All images, categorizations, and justifications based on CL relationships are compiled in the Appendix. To extend the reach of our CL analysis, we compiled our newly collected CL images with a collection of previously published CL images of quartz-hosted embayments (Appendix). This compilation includes CL imagery for 18 new embayments collected for this study alongside 159 additional CL images collected from the literature. Final counts include both data suites. We conclude that embayments may form by either dissolution or growth (Figure 2.5). From a collection of 178 embayments, we found that 25% form by growth,

43% form by dissolution, and 31% could not be determined from the images because of poor image quality or lack of clear banding in the embayment vicinity.

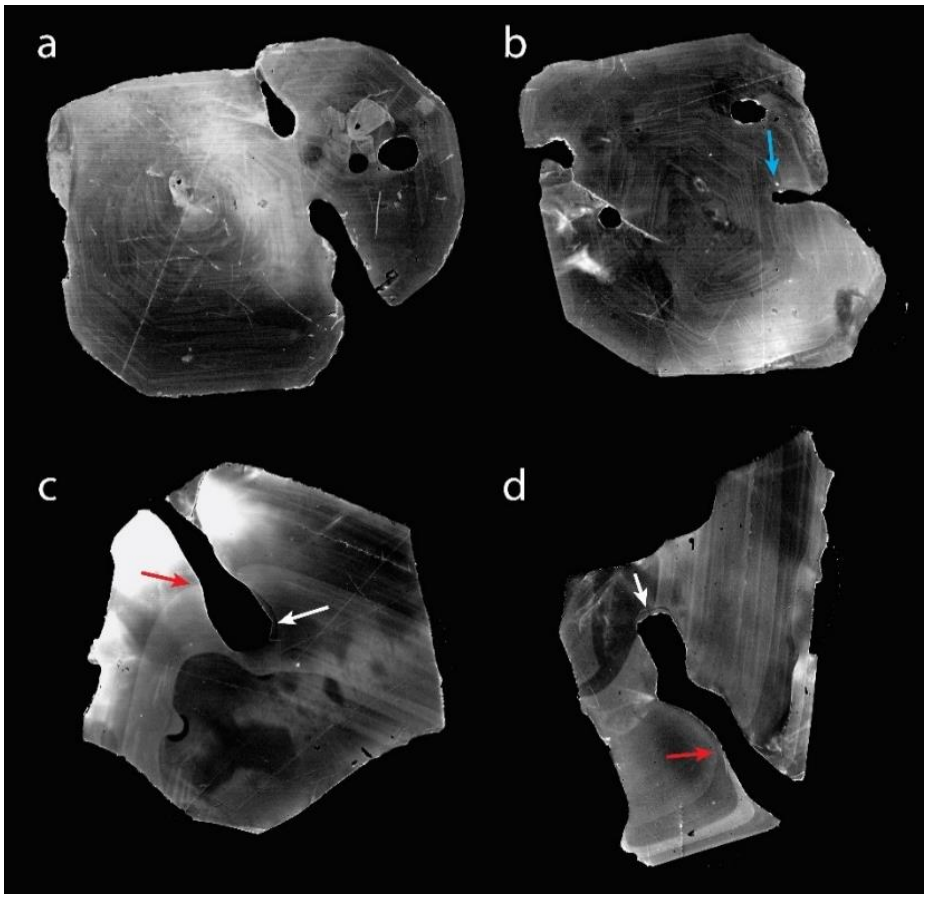

Figure 2.4. a) Cathodoluminescence (CL) image of a Bandelier Tuff quartz crystal, with two embayments formed at the contact between two ingrown crystals; b) quartz from the Bandelier Tuff; blue arrow indicated dissected CL bands; c) quartz from the Huckleberry Ridge Tuff (HRT); red arrow indicates deflected growth bands, white arrow highlights faceted embayment interior; d) quartz from the HRT with deflected growth bands (red arrow).

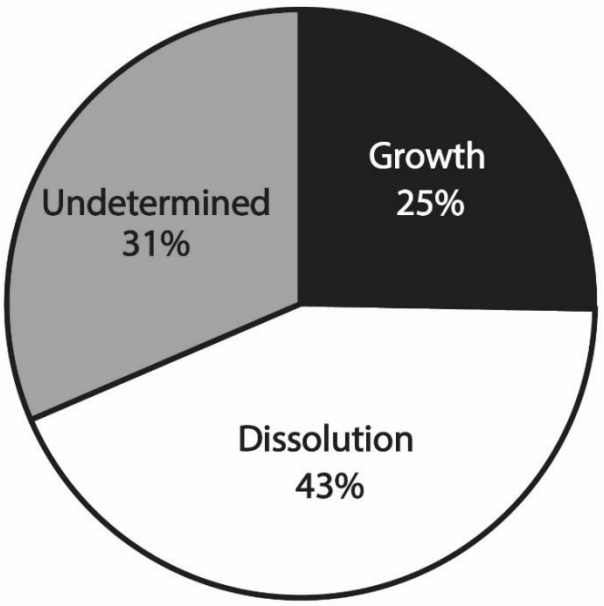

Figure 2.5. Pie chart showing results from CL analysis of embayments in quartz prepared for this study and those compiled from the literature (n = 178 embayments).

Embayments are filled with glass and bubbles, and combinations thereof. This filling character does not correspond to embayment size or morphology in any of the targeted eruptions. The filling character of quartz-hosted embayments can be categorized into four classifications: dense glass, intruding bubble, discrete bubbles, or decrepitated (Figures 2.1, 2.6). Dense embayments are fully filled with glass with no bubbles. Intruding bubbles continuously extend from the embayment interior into the vesiculated pumice external to the quartz crystal. This category has varying amounts of embayment glass. In some, a smaller bubble only partially fills the embayment, whereas others have a relatively large bubble that volumetrically dominates the embayment. The discrete bubbles category has isolated bubbles contained entirely within the embayment and the bubbles are surrounded by glass. We identified 2 sub-categories of discrete bubbles: elongate and free-floating. Discrete, elongate bubbles are similar in shape to intruding bubbles but are distinguished by an isthmus of glass that fully isolates the bubble within the embayment's interior. These bubbles do not extend into vesiculated pumice exterior

to the quartz's surface. Discrete, free-floating bubbles are spherical and are fully enclosed within embayment glass. Free-floating bubbles may be attached to crystal walls or entirely enveloped by glass. Decrepitated embayments are opaque, dark brown to black in color, and preserve no distinguishable bubble textures. Empty embayments are hollow cavities in the quartz host (e.g., Lava Creek Tuff examples from Befus and Manga, 2019).

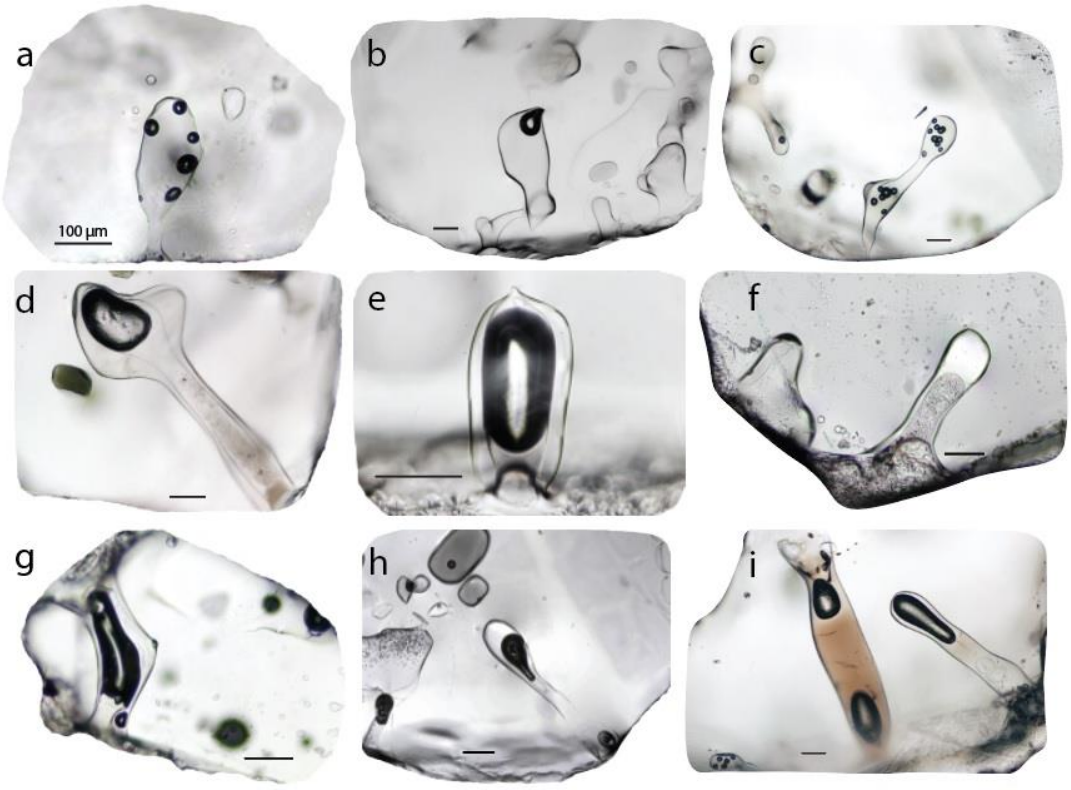

Figure 2.6. Photomicrographs of embayment filling characteristic textures; discrete free-floating bubbles occurring in: a and c) multiples and as a b) single, lone bubble; d-f) intruding bubbles which penetrate the full length of the embayment glass. Some index of refraction differences are complicated by mineral oil partially filling the intruding bubble. g-i) discrete elongate bubbles which are similar to intruding bubbles, yet are discontinuous and truncate inside the embayment. Scale bar in each panel is 100 µm.

Quartz-hosted embayments are common features in all eruptions and all forms (Figures 2.7-8). Empty embayments were recognized so rarely across the targeted

eruptions that they were excluded from the characterization and counts. Across all eruptions, the dense glassy texture was the most common, followed by intruding bubbles and discrete, free-floating bubbles (Figure 2.9). We specify the diversity in bubble textures for each eruption in the following subsections.

Bandelier Tuff, Valles Caldera

Quartz crystals from the Valles caldera system were collected from the Tsankawi Pumice (RCE-B), the initial Plinian phase of the Upper Bandelier Tuff. The Tsankawi Pumice lies stratigraphically between the Tshirege and Cerro Toledo Formation. Tsankawi Pumice contains up to 30 vol.% phenocrysts, primarily comprised of quartz and sanidine (Dunbar and Hervig, 1992). Quartz are predominantly euhedral, beta quartz bipyramids. Of all samples analyzed in this study, the Bandelier Tuff contained the highest number of unfragmented grains. 85% of the quartz phenocrysts contain one or more embayments, which is the greatest abundance of embayed crystals across our suite of large silicic eruptions. Most of the embayments are glassy (62%). Bubble-bearing embayments are less common and we observe 15% have intruding bubbles, 12% have discrete, free-floating bubbles, 8% contain elongate bubbles, 2% are empty, and 2% are decrepitated.

Oruanui Tuff, Taupo Caldera

The Oruanui Tuff from Taupo caldera in New Zealand is a quartz-poor rhyolite. Whole-rock crystallinity in rhyolite samples from this eruption range from 3-13% (Wilson et al., 2006). The largest quartz in the Oruanui Tuff pumice samples were found

in the 500-710 μm size fraction. Many crystals are highly fractured, but these were avoided when possible. Only 34% of quartz were embayed. The population of quartz was comprised of nearly equal proportions of dense glassy embayments and those with intruding bubbles, 44% and 48% respectively. The remainder was 5% free-floating bubbles and 3% with elongate bubbles. No embayments were empty or decrepitated. Two different eruptive units (F1 and F2) of the Oruanui Tuff were assessed independently to examine differences across eruptive pulses. Additionally, counts from two individual, whole pumices from F1 collected at two different locations were chosen for comparison between individual pumices and site localities. Embayment proportions were consistent between pumice clasts collected from separate sample locations, individual pumices, and units. Counts from all units were thus combined and reported together.

Eruptions from Yellowstone Caldera

We examined embayment textures in 3 large-volume, pyroclastic eruptions from the Yellowstone caldera system. Airfall material was the source for quartz from the Huckleberry Ridge Tuff and Mesa Falls Tuff, whereas Tuff of Bluff Point quartz were extracted from pumice clasts from a loose, unwelded ignimbrite deposit.

Quartz crystals from the Huckleberry Ridge Tuff contain fractures, but many have not fragmented. Huckleberry Ridge Tuff quartz are highly embayed with 71% of all crystals containing at least one embayment. Within the embayed group, dense glassy embayments and intruding bubbles dominate the observed textures, at 49% and 39% respectively. When glassy, embayments commonly preserve a clear to light-yellow color gradient. Glass deep in the interior is the lightest shade, which becomes progressively

more saturated towards the exterior. We see no correlation between bubble content, microlites, or glass color. Minor textures include discrete free-floating bubbles (3%), elongate bubbles (1%), and decrepitated (8%). No empty embayments were observed. Sometimes Huckleberry Ridge Tuff embayments fully penetrate the interior of a crystal, meaning the embayment has at least 2 openings. This is a rare morphology within our full suite samples, but it occurs with unusual frequency in the Huckleberry Ridge Tuff quartz.

The Mesa Falls Tuff contains large, euhedral, bipyramidal beta quartz. 53% of crystals examined contain at least one embayment. Dense, glassy embayments are the most common, accounting for 49% of observed textures. Like the Huckleberry Ridge Tuff, some dense glassy embayments from the Mesa Falls preserve color gradients. When found, these gradients tend to grade from yellow to brown. Intruding bubble textures are common, occurring at 41%. All other textures are infrequent, with 3% free-floating bubbles, 1% elongate bubbles, and 7% decrepitated.

Quartz from the Tuff of Bluff Point are the second-most embayed, with 82% of crystals containing embayments. Tuff of Bluff Point quartz also commonly contain multiple embayment textures in single phenocrysts. The majority of embayments are dense glass (43%) that may be clear, brown, or have gradients from clear to brown. Bubbly textures are recognized in ~30% of the embayments, occurring as intruding bubbles (12%), free-floating bubbles (11%), and elongate bubbles (5%). The remaining ~30% of the embayments are opaque and decrepitated. The abundance of decrepitated embayments cannot solely be attributed to relatively slow post-eruptive in an ignimbrite because some crystals host decrepitated embayments immediately adjacent to dense, glassy embayments.

La Primavera Caldera

A single, 10-cm diameter pumice clast from the La Primavera Giant Pumice Horizon was crushed and picked for quartz. The Giant Pumice Horizon was emplaced by a subaqueous eruption within the La Primavera caldera (Sourisseau et al, 2020). Quartz phenocrysts in this unit are rare, rounded, and small. Most phenocrysts occurred in the 355 to 500 µm size fraction. Embayments are ubiquitous in the La Primavera quartz, appearing in 69% of the examined crystals. Embayments, and melt inclusions, are notably clear, dense, and bubble-free. 73% of embayment textures are dense and glassy. Bubbles within embayment glass are less prevalent in this eruption, with only 20% containing intruding bubbles, 4% elongate bubbles, and 2% free-floating bubbles. No empty or decrepitated embayments were observed.

Bishop Tuff, Long Valley Caldera

We assessed quartz-hosted embayments from pumice clasts from the Bishop Tuff's fall deposits and ignimbrite. Quartz from initial fall deposits F1-F3 have embayments in 37% of crystals. Approximately half of the embayments are dense glass (47%). The remainder of have bubble textures. Intruding bubbles comprise 37% of the population, followed by free-floating (13%), elongate (4%), and decrepitated (2%). Discrete, free-floating bubbles tend to occur as a single, isolated bubble rather than in clusters or multiples. Just over half of the quartz inspected from the Bishop Tuff Ignimbrite (Ig2Ea) sample contained embayments (55%). Of those, 39% of these were glassy, 31% contained intruding bubbles, free-floating bubbles followed closely with

28%, and elongate bubbles accounted for only 3% of total textures. No decrepitated embayments were seen in the ignimbrite, but they were also rare in the fall. Empty embayments were not observed in any Bishop samples.

Younger Toba Tuff, Toba Caldera

Blocks of welded Younger Toba Tuff ignimbrite were crushed and picked (sample was collected at Teles field trip stop 2.4 by S. Self on the field trip associated with the 2018 IAVCEI International Workshop on Collapse Calderas). Quartz in this sample is highly fragmented. Our counts from this eruption represent minimums as fragments may have contained additional embayments that are now lost. Embayments composed of dense, clear glass are rare (14%). Bubble textures are far more prevalent, with intruding bubbles accounting for 33% of observed textures, followed by discrete elongate (26%), free-floating (21%), and decrepitated (5%).

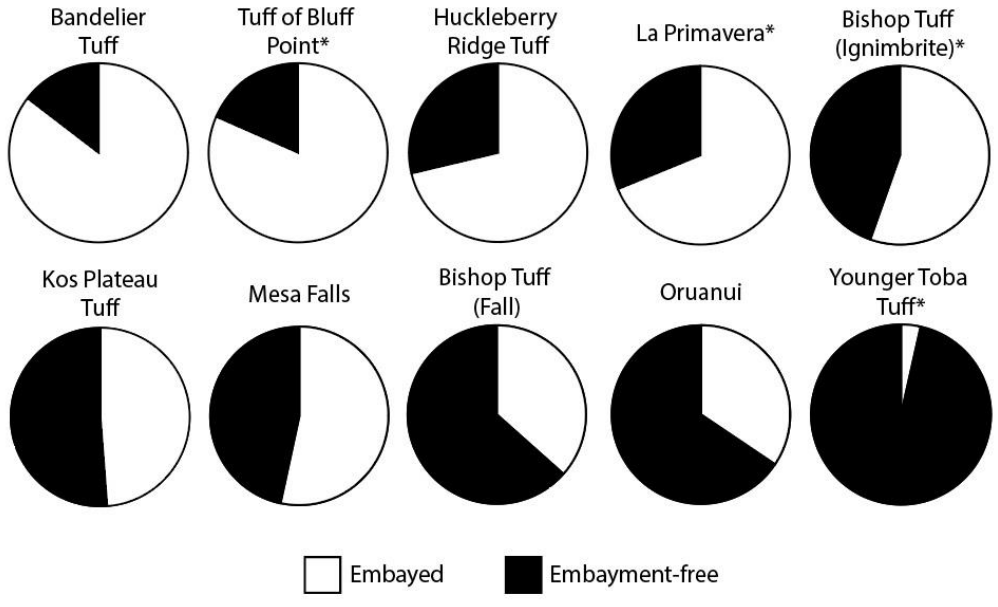

Figure 2.7. Percentage of crystals with embayments from each eruption. Samples from ignimbrites are indicated with an asterisk. Data are in Table 2

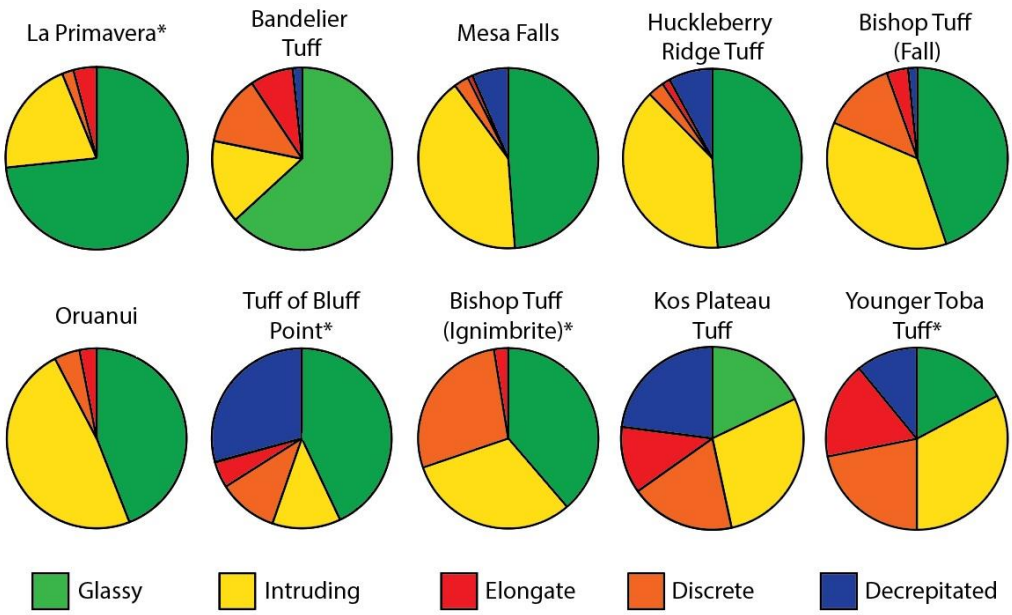

Figure 2.8. Relative abundance of embayment morphologies.

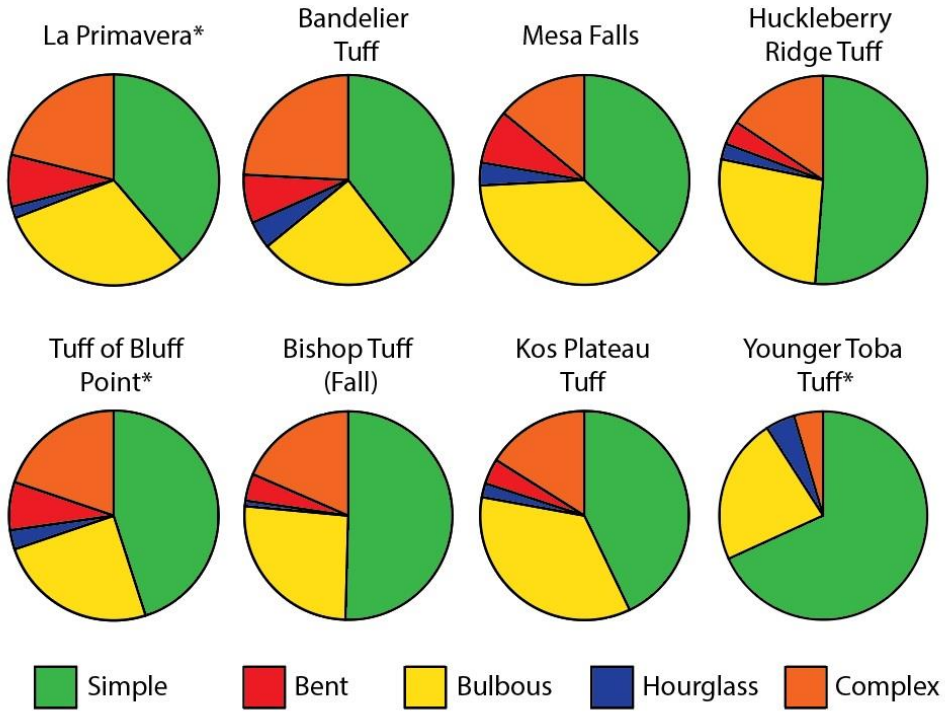

Figure 2.9. Relative abundance of bubble textures within embayments.

Discussion

Embayments are common features in quartz from large silicic eruptions. Nearly all quartz are embayed in some eruptions (e.g., the Bandelier Tuff, Tuff of Bluff Point), whereas they are scarce in others (e.g., Younger Toba Tuff). Although the absolute abundance of embayed quartz varies by eruption, the diversity and proportions of embayment morphology is shared among all the studied units. The consistent pattern we find is simple>bulbous>complex>bent>hourglass. The most geometrically simple embayments occur the most commonly. Increasingly complex forms have larger surface area to volume ratios. The surfaces of all quartz-embayment contacts are smooth and curved. They lack angular, faceted faces that would be associated with crystal growth. The free energy of rounded quartz-embayment contacts is high and indicates embayments are a product of disequilibrium in the magma reservoir.

Relict disequilibrium textures can be exploited using kinetics to extract meaningful timescales of magmatic processes (e.g., Watkins et al., 2012; Andrews and Befus 2020). The diffusion-limited volatile concentration gradients in embayment glass that can be used to estimate magmatic ascent rates are a significant and topical example (e.g., Myers et al., 2016; 2018; 2021; Liu et al., 2007). Here, the rounded quartz-embayment surfaces recognized in all of the large silicic eruptions may be a second timescale that records the duration between embayment formation and eruption. Rounded quartz surfaces will progressively facet as they grow and approach equilibrium (Gualda et al. 2012; Pamukcu et al. 2015). Using faceted to partially-faceted melt inclusions, Pamukcu et al. (2015) demonstrated that quartz grew over 10 to 600 years in the Oruanui, Ohakuri-Mamaku, and Bishop Tuffs. Timescales from rounded embayments must be shorter because they are unfaceted. Quartz-hosted embayments should begin to facet in

<100 years (Gualda et al. 2012; Pamukcu et al. 2015). The absence of faceting indicates the process that produces and maintains embayments is active in the years to decades immediately preceding eruption.

Because the diversity and proportion of embayment morphologies are consistent across the ten eruptions considered here, we conclude there is a shared process that produces embayments in rhyolitic magmatic systems. Embayments may form by crystal growth or dissolution, and there is no current consensus. Those that favor a crystal growth mechanism attribute embayment form to rapid, skeletal growth (e.g., Roedder, 1979; Loewen et al., 2017; Barbee et al., 2020). Others favor a dissolution mechanism produced when an exsolved volatile bubble attaches by surface tension to the quartz-melt interface, and subsequently drills into the phenocryst (Busby and Barker, 1966; Donaldson and Henderson, 1988; Harris and Anderson, 1984; Befus and Manga, 2019). Quartz-hosted embayment surfaces are curved and irregular, which are a high energy, disequilibrium texture. Embayments also commonly have single, external bubble located at the crystal-melt interface. Elevated volatile concentrations in and around such bubbles would produce thermodynamic disequilibrium and enhance crystal dissolution (Busby and Barker, 1966). Finally, crosscutting relationships between CL bands and quartz-hosted embayments have been documented in many silicic eruptions (Supplemental Fig 1) (e.g., Liu et al., 2006; Vazquez et al., 2009; Girard and Stix, 2010; Matthews et al., 2012; Peppard et al., 2001; Loewen and Bindeman, 2017; Pamukcu et al., 2015; Gualda et al., 2012).

We collected CL images of quartz marked by various embayment morphologies. We combined this with all known, previously published CL imagery of embayment-

hosting quartz. We find that dissolution is the primary mechanism, accounting for 43% of the dataset. Growth, though still common, accounts for only 25%. The formation mechanism for the remaining 31% could not be determined with confidence. Thus, embayments form commonly via both dissolution and growth.

Glass and bubble textures preserved within embayments provide additional insight to the formation of embayments in the magma reservoir. Dense, glassy embayments are the most common filling texture in quartz from silicic eruptions. In 7 of the targeted eruptions they account for the largest proportion of embayments. This result supports and lends credibility to embayment speedometry studies, which rely upon the calculation of a decompression timescale from volatile diffusion profiles preserved in the dense glass. Descriptions of dense, glassy embayments may be overrepresented, but we confirm they are indeed an important and characteristic texture produced in magma reservoirs.

Bubble textures are also commonly found in embayments. Bubbles are recognized in all studied eruptions. Quartz from some eruptions, like the Oruanui Tuff and Younger Toba Tuff, are dominated by bubbly embayments. Bubbles within embayments may be vestiges of pre-eruptive bubbles or form in response to supersaturation during magmatic ascent. Pre-eruptive bubbles have been shown to exist in many silicic systems (e.g., Wallace et al., 1995; Gualda and Anderson, 2007; Steele-MacInnis et al., 2017). For example, melt inclusions may contain pre-eruptive bubbles which are too large to have been formed solely via shrinkage during quench (e.g., Allison et al., 2020). Embayments contain bubbles that occupy up to 90 vol.%. By comparison with inclusions, it is likely that some of the bubble-filled volume in embayments represents pre-eruptive, exsolved

fluid. Intruding bubbles are the most common texture. Because intruding bubbles extend from the external melt into the embayment channel, they result from, or at least are modified by, bubble growth during conduit ascent.

The presence, or absence, of dense glasses and bubbly textures have important implications for pressure within embayments. Bubbles nucleate and grow in magmatic melts in response to volatile supersaturation and decreasing pressure. Bubble sizes and number density in those melts reflect ascent rates and conditions (e.g., Hajimirza et al., 2021; Toramaru, 2006). Bubble nucleation and growth kinetics have been demonstrated experimentally to be rapid, however, fast ascent rate can outpace them leading to supersaturation and disequilibrium (Mangan and Sisson, 2000). The required ascent rates for supersaturation are so fast that diffusion-limited volatile profiles would not form. Embayment speedometry shows this is not the case. In addition, embayments preserve dense glass without bubbles. This demonstrates that melt trapped in quartz-hosted embayments does not vesiculate in the same fashion as free melt in the conduit.

To suppress bubble nucleation and growth, dense melt within embayments must experience a different decompression history than free melt in the conduit. We explore the possibility of suppression by viscous shielding to explain embayment bubble textures, and lack thereof. Qualitatively, small embayment channels and/or high viscosity melt could maintain a barometric disequilibrium in the embayment that manifests as an overpressure that suppresses vesiculation. To quantitatively explore the fluid dynamic possibility of such viscous shielding in embayments we applied the principles of Poiseuille flow for a viscous fluid through a channel with no-slip boundary conditions. The concept for this model was first established by Anderson, 1991 and applied to

embayments with very thin, constricted necks (hourglass inclusions). We build upon the concepts of this work for embayments with varying geometries.

Here, the channel in the embayment is defined as the neck region in diameter (d) and length (l) (Figure 2.10). The flow is laminar as the low velocities and relatively high viscosities lead to very small Reynolds Numbers (10^{-21}—10^{-9}). We assume an isothermal environment and that melt in the conduit and embayment are in equilibrium initially. Pressure is calculated at each timestep (1 s) for the embayment and conduit melt.

The model runs until the conduit melt reaches a prescribed fragmentation depth (e.g., 300 m) or the embayment melt is completely evacuated, whichever occurs first. Melt flows through the embayment neck in response to changes in pressure.

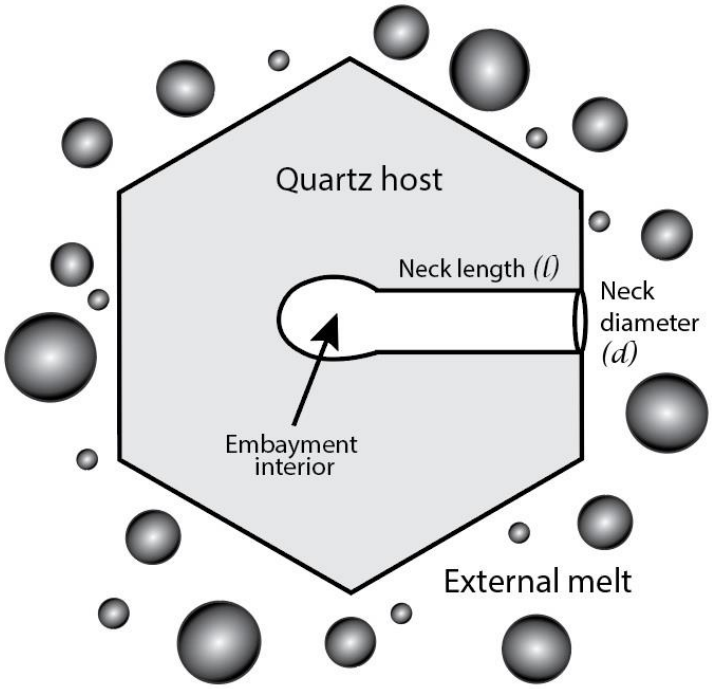

Figure 2.10. Embayment schematic illustrating model conditions (modified from Liu et al., 2007).

The overall embayment pressure (P_{emb}) is calculated as a linear relationship between the fraction of melt and bubbles in the embayment:

$$(1) \qquad P_{emb} = \left[P_{emb-1} \cdot \left(1 - \frac{Q}{V_{emb}}\right)\right] + \left[P_{melt} \cdot \left(\frac{Q}{V_{emb}}\right)\right]$$

Where P_{emb-1} is the previous embayment pressure, V_{emb} is the embayment volume, and P_{melt} is the magmastatic pressure in the melt that scales with depth.

Highly viscous, silicic melt cannot flow fast enough through the neck to maintain equilibrium. A pressure gradient is thus produced across the embayment, such that melt in the embayment maintains a higher pressure than melt in the conduit. Overpressure within embayment melt will suppress bubble nucleation. Embayments are typically far less vesicular than pumice from the same eruption, a common observation documented widely in the literature. We predict that embayment geometries always viscously shield interior melt during ascent. Faster decompression rates preserve greater overpressures. A similar effect can be produced independently by smaller embayment diameters, longer embayment necks, or higher melt viscosity (Figure 2.11). Overpressures become more pronounced as magma ascends higher in the conduit and viscosity increases. Overpressure will impact diffusive degassing. Volatile gradients preserved in embayments may not solely reflect diffusive loss in response to decompression in the conduit, but also the pressure gradient produced by viscous shielding. A quenched, erupted embayment may thus contain a diffusion profile which records pressures greater than the conditions of shallow fragmentation. It is also possible that flow may occur in reverse, allowing melt to refill embayment pockets. Together, these possibilities present complications for the interpretation of diffusion profiles.

Our calculations illustrate that embayments can lose melt by viscous flow. The amount of melt loss is an additional timescale that may be reflected in embayment bubble textures. Melt loss is predicted to increase with shorter embayment lengths, wider neck diameters, and slower ascent rates. Viscous flow calculations indicate that the volume of melt retention approaches 100% at ascent rates >1 m s^{-1}, in good agreement with some ascent estimates ranging up to 10 m s^{-1} from volatile concentration gradients in dense, glassy quartz-hosted embayments (Myers et al., 2016; 2018; 2021). Slower ascent rates <0.5 m s^{-1} provide ample opportunity for melt loss. For very short embayments, or those with neck diameters >50 μm, full evacuation may occur even at slower ascent rates. The agreement with diffusion timescales fails at these slow rates. Some dense, glassy embayments preserve diffusion-equilibrated volatile gradients produced by ascent as slow as 0.1 m s^{-1}, which our model would predict should be fully empty (Myers et al., 2016; 2018). In addition, each eruption contains embayments with diverse bubble textures. Sometimes a single crystal preserves a wide range in bubble volume in the embayments. Clearly, complications are occurring in the natural system that are not accounted for in our simple model. We acknowledge that the viscous flow model does not comprehensively describe embayment conditions but maintain that it provides an interesting first-order, quantitative framework for improving our understanding embayments and interpreting natural textures.

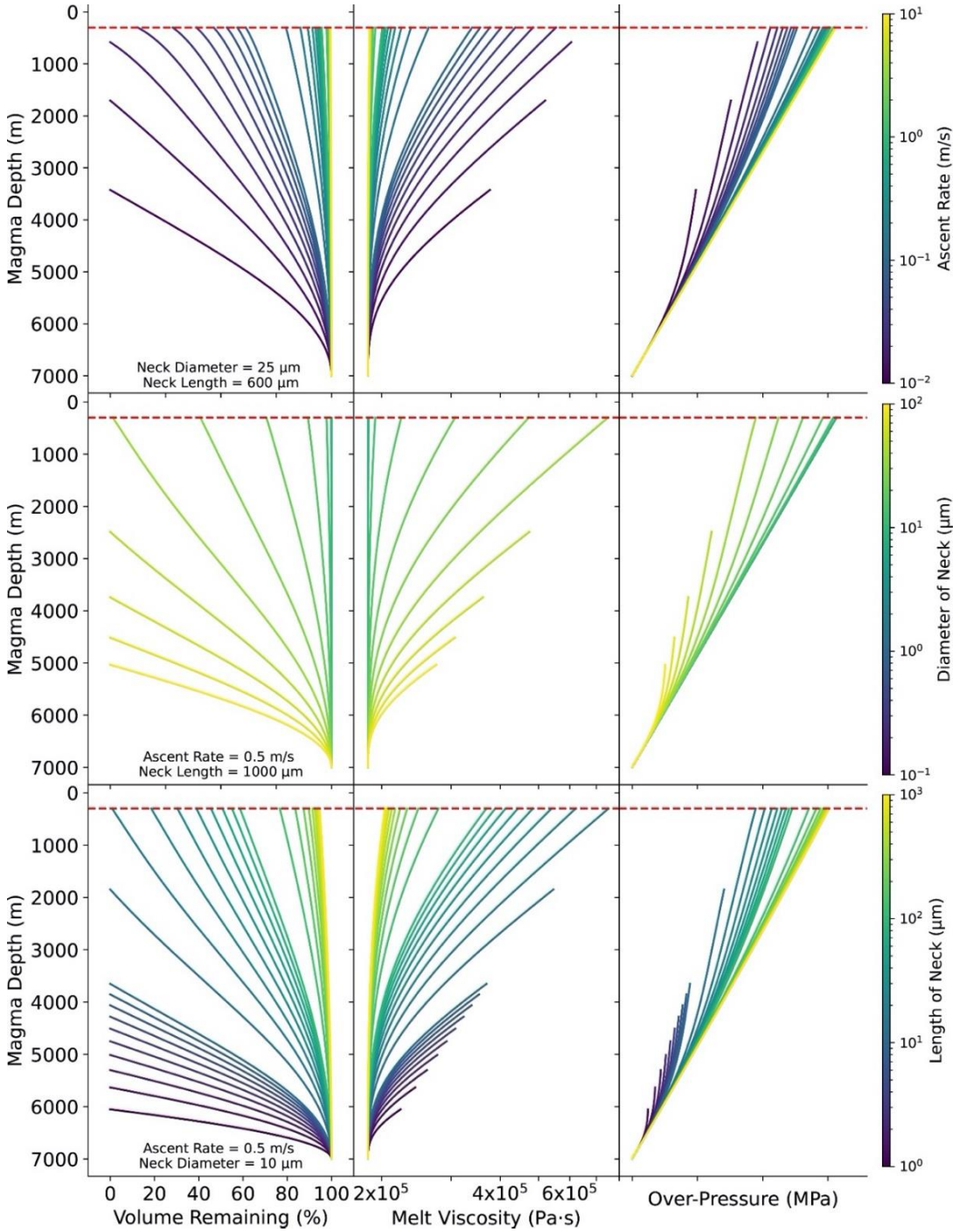

Figure 2.11. The influence of embayment (a) neck diameter, (b) neck length, and (c) ascent rate on volume of melt remaining, melt viscosity, and over-pressure in the embayment during ascent in a magma body for a high silica rhyolite. The dashed red line indicates the fragmentation depth (300 m).

Conclusion

Embayments are clocks that may record three separate timescales. Embayment speedometry is becoming a well-established technique and has seen its application grow significantly in the past 20 years. Embayments record magmatic decompression in the diffusion-limited volatile gradients preserved within dense, glassy embayments. These concentration profiles recover final ascent timescales on the order of minutes to hours. More temporal information can be extracted from other disequilibrium textures in embayments. Rounded, unfaceted embayments record the time from their formation leading up to eruption. This timescale must be shorter than that required for faceting, on the order of years to decades prior to eruption (Gualda et al., 2012; Pamukcu et al., 2015). Bubble textures reveal a third timescale, associated with viscous flow, shielding, and eruptive ascent. Numerical modeling of viscous flow indicates bubbles could form as melt evacuates during ascent. The emptying/bubble-forming process is operating synchronously with diffusive re-equilibration of volatiles in embayment melt. Both processes are dependent upon one another. The resulting independent timescales should match, and they do at the fastest ascent rates. The similarity breaks down at rates less than 1 m s^{-1}. Our modeling does not fully reconcile these timescales, but it suggests embayment-scale variations which may be further explored and exploited.

CHAPTER THREE

Experimentally Testing Embayments as Record Keepers of Magmatic Ascent

Introduction

Experiments are needed to validate petrologic tools. Experiments help users recognize unforeseen complications or exploit additional opportunities in the rock record. Speedometers are a style of petrologic tool that uses preserved disequilibrium textures to infer a timescale for a volcanic or magmatic process. A significant example is that of bubble and microlite number densities in volcanic rocks (Toramaru, 2006, 2008; Gardner, 2007). Experiments have illustrated a relationship between decompression rate and the number of bubbles or microlites present in a volume of melt. The textures within pumice erupted during Plinian events is consistent with those present in experimentally, rapidly decompressed magma (Hamada et al., 2010). Experiments additionally reveal that the form of the decompression pathway (linear, exponential, etc.) also influences observed textures (Befus and Andrews, 2018). Many other petrologic tools have been developed, and the community is always searching for new tools to learn more about volcanic and magmatic processes (Rutherford and Hill, 1993; Wolf and Eichelberger, 1997; McCanta et al., 2007).

Embayment speedometry is one of the most recent tools developed by the volcanological community, only emerging in the past ~10 years. As such, the method remains experimentally untested, yet it continues to grow in popularity and applicability. It has been applied in a total of 9 studies that have interrogated the timescales preserved

with a total of 75 crystals. Approximately 1-2 studies are published each year using this method, with 2 already published this year (e.g., Myers et al., 2021; deGraffenreid and Shea, 2021).

Importantly, embayment speedometry is not validated by any experiments, relying solely on diffusion theory and numerical modeling. Embayment speedometry additionally relies on the assumption that a few crystals are capable of fully recording the complexities of magmatic ascent during an eruption. Furthermore, it requires the exclusive use of embayments with ideal, cylindrical geometry. Embayments are assumed to have a bubble at the embayment mouth to ensure sufficient diffusive exchange with the melt. Models for the diffusion profiles within embayment glass are increasingly accounting for additional complexities (deGraffenreid and Shea, 2021), but robust experimental verification remains outstanding.

To address this, I developed an experimental approach to assess embayment speedometry. The goal of this approach was to produce dense, glassy quartz-hosted embayments that preserve a diffusion-limited H_2O profile that reflects the experimentally imposed decompression rate. I ran experiments in a cold seal high temperature lab at Baylor University using rhyolite melt in both natural and synthetic quartz hosts. I successfully demonstrated that simple, cylindrical synthetic embayments with ideal dimensions can be drilled into quartz cores. Filling these synthetic embayments with dense, bubble-free glass, however, has proven challenging. Natural quartz-hosted embayments are commonly filled with dense glass, it remains unclear why I have been unable to duplicate that texture. I did succeed in experimentally erasing diffusion profiles in embayments in natural crystals by running experiments at temperature and pressure

conditions to attain much higher H_2O solubility. In all other experiments, the quartz-hosted embayments vesiculate persistently and significantly during decompression. This approach yields very few dense, glassy embayments and does not fully replicate textures observed in nature. In this chapter, I detail the experimental methods undertaken and highlight the few successes and many challenges that will confront future researchers on this topic.

Methods

Quartz cores for synthetic embayment microdrilling were prepared by first coring a block of synthetic quartz into 2 mm diameter cylinders between 4 to 7 mm in length. The cylindrical cores were then ground and polished on opposite sides to produce two parallel, flat faces. Cores were shipped to LightPulse Laser Precision, a manufacturing startup specializing in ultra-short pulse laser material processing based in Stuttgart, Germany. The use of ultra-short pulse lasers allowed for precise drilling of holes into the quartz, which we will exploit as synthetic embayments. In each of the 20 cores, 5 cylindrical holes were sunk into one of the flat faces. Holes were ~100 ±10 μm in diameter and ~500 ±10 μm in length. The holes thus had a controlled, simple geometry that is similar in dimension to many ideal, natural quartz-hosted embayments. Drilled holes were aligned along a plane, with respect to each other, to allow for simultaneous double exposure of all 5 synthetic embayments during sample preparation and more efficient analytical work (Figure 3.1).

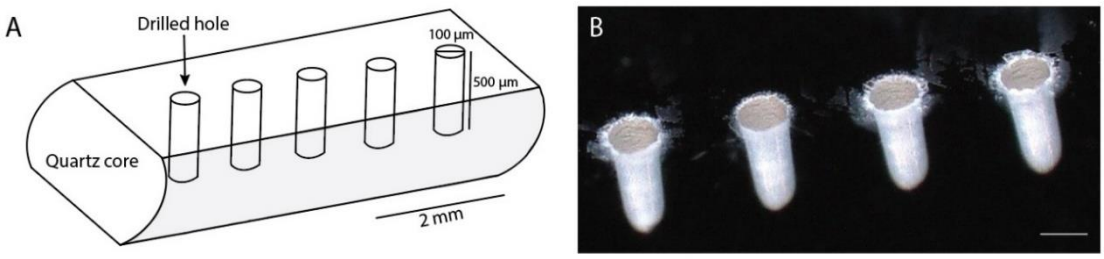

Figure 3.1. a) Schematic illustrating a drilled core; b) photomicrograph of successfully drilled cores in quartz core; scale bar is 100 µm.

The second starting material was embayment-bearing quartz phenocrysts picked from the Bishop Tuff and Huckleberry Ridge Tuff, from Long Valley caldera, CA and Yellowstone caldera, respectively. For these experiments, up to 20 quartz phenocrysts containing dense, glassy embayments were included in a single experiment. Typically, ~30% of the natural embayments in an experiment will survive the experiment and can be extracted for sample preparation. Of these, some are either lost or destroyed while mounting crystals, grinding, and polishing. This approach is challenging because many crystals are lost. The strengths of the technique, however, are the opportunity to test naturally complex embayment shapes and the independence from expensive laser drilling preliminary steps. Both methods are complimentary, presenting the prospect to test natural, complex and simple, synthetic embayment geometries.

To experimentally test the fidelity of the embayment speedometry tool, I performed a series of high temperature experiments using the cold seal high temperature lab. Experiments were run with synthetic embayments and re-equilibrated natural embayments at magmatic conditions and known decompression rates. To run experiments, I first loaded natural and synthetic embayments into Au or Pt capsules with aliquots of rhyolite powder. Sufficient H_2O was added by syringe to each capsule to

ensure the rhyolite melts were at the correct level of saturation, typically 4-5 mg. Then, the capsules were welded and sealed. Capsules were then loaded into a cold-seal Waspaloy pressure vessel along with a steel filler rod. The steel filler rod controls oxygen fugacity at reduced conditions below the QFM buffer. Reduced oxygen fugacity prevents crystallization of Fe-Ti oxide microlites and results in optically clear rhyolite glass. The fully loaded pressure vessels were then cold-sealed with a large wrench, connected to the hydraulic pressure line, and finally inserted into a box furnace. We ran experiments in two steps at magmatic conditions. We first hydrate the rhyolite melt in the experiments to be equilibrated at ~4 wt. % H_2O, staying below solubility of 6 wt. % H_2O at 740-800 ^oC and 200 MPa. (Liu et al., 2005). Equilibration of H_2O takes less than 24 hours at experimental conditions. Establishing this initial equilibrium H_2O concentration throughout the sample is an important first step for later diffusion modeling of gradients that should be producing during decompression.

Following equilibration, the experiments may be decompressed to simulate magmatic ascent. To achieve a continuous, linear decompression pathway, we use a calibrated pressure actuator. The pressure actuator is a temperature-controlled, large-volume pressure vessel that is open to the pressure line. Cooling the actuator reduces the volume of the water in the actuator, which in turn lowers the pressure in the system at a rate that correlates with cooling rate. This process allows controlled decompression from a starting pressure of 200 MPa to a final, quench pressure of 30 MPa. The quench pressure of 30 MPa was chosen to limit the effect of vesiculation at low pressures. At this final pressure we expect water solubility in the melt to have dropped to 2 wt. % H_2O (Liu et al. 2005).

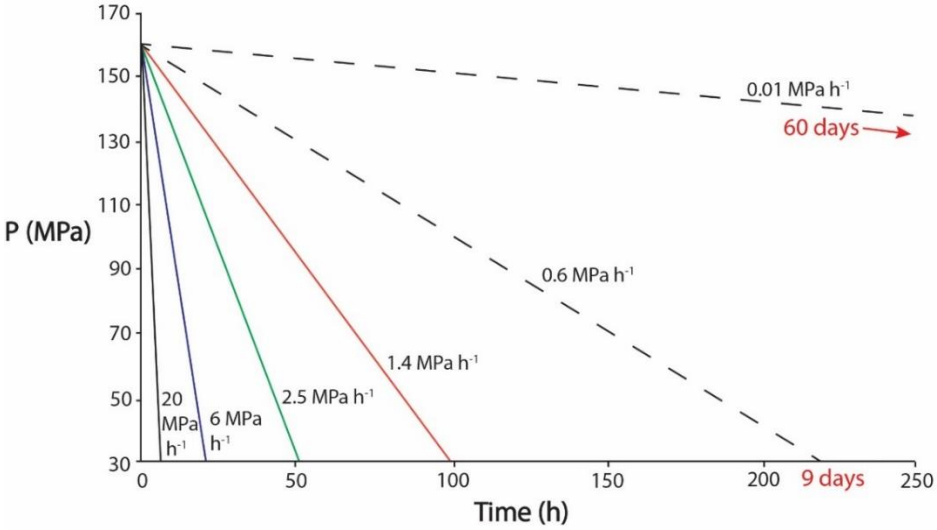

Figure 3.2. Experimental decompression pathways. Colored, solid lines represent actual data from preliminary experimental runs for faster decompression on the order of hours to days. Dashed, black lines represent much slower decompression rates over the course of days to months for future experiments. This is MPa per hour rather than second, like in the introduction.

To quench, I first blow compressed air on the >700 ^{o}C sample-hosting pressure vessel to start the cooling process, and then we completely submerge it in a bucket of water. This process quenches the sample to temperatures below the glass-transition in under 30 seconds (Waters et al., 2015). Natural embayments are run at the same decompression pathways. Decompression rates between 100 and 0.01 MPa h^{-1} were explored (Figure 3.2). These rates represent magmatic ascent timescales from hours to months, enabling us to test the effectiveness of embayment geospeedometry applied to rapid, intermediate, and slowly evolving eruptions.

Results and Discussion

To date, 18 experiments have been conducted to develop an experimental methodology to test embayment speedometry (Table 3.1). Most of these experiments are hydration of synthetic cores and natural embayments. The remainder are decompression experiments using natural embayments.

Table 3.1. Starting conditions, materials, and results from each experiment compiled.

Experiment	Core or natural?	# of xls	Wt. % H_2O	Capsule contents	P_i (MPa)	P_f (MPa)	T (°C)	t (hrs)	Decompression Rate (MPa s^{-1})	Result
R1	Natural	20	4.5	Powder	200	20	800	15	N/A	None recovered
R2	Core	N/A	4	Powder	215	21	800	24	0.002	Synthetic embayments not filled
R3	Core	N/A	Saturated	Powder	200	36	800	5	0.006	Synthetic embayments highly vesiculated; flat diffusion profiles
D1	Natural	20	Saturated	Hydrated obsidian	160	30	800	22	0.001	Embayments fully vesiculated
D2	Natural	11	4	Powder	160	36	800	48	0.001	80% of embayments vesiculated
D3	Core	N/A	Saturated	Powder	170	35	800	96	0.001	Synthetic embayments highly vesiculated; flat diffusion profiles
NE4	Natural	21	5	Powder	180	35	800	26	0.002	80% of embayments vesiculated
NH5	Natural	18	5	Hydrated obsidian	200	200	800	96	N/A	None recovered
CE1	Core	N/A	5	Hydrated obsidian	200	200	800	72	N/A	Synthetic embayments not filled
CE1.2	Core	N/A	5	Hydrated obsidian	200	200	800	25	N/A	Synthetic embayments not filled
CE2	Core	N/A	5	Hydrated obsidian	200	200	800	72	N/A	Synthetic embayments not filled
CE3	Core	N/A	5	Hydrated obsidian + powder	200	200	800	72	N/A	Synthetic embayments not filled
CE3.1	Core	N/A	5	Hydrated obsidian + powder	222	250	800	96	N/A	Synthetic embayments partially filled (~30%)
CE4	Natural + Core	3	4	Hydrated obsidian + powder	220	220	825	96	N/A	Synthetic embayments partially filled (~30%); successful diffusion profile from 1 natural embayment.
CE5	Core	N/A	5	Hydrated obsidian + glass shards	220	220	825	168	N/A	Some synthetic embayments partially filled, some empty
CE6	Core	N/A	5	Powder	200	200	800	168	N/A	Partially filled (~60%); highly vesiculated
CE6.1	Core	N/A	Saturated	Powder	210	210	750	192	N/A	Experimental capsule unwelded; core shattered; synthetic embayments partially filled

Filling and Hydration Experiments

The initial condition for validation experiments is dense, glass filling embayments. If achieved, these embayments could be used for decompression experiments. Creating the perfect synthetic dense filled embayments was never achieved here. Instead, many experiments vesiculated. One potential culprit is the viscosity of the melt. Rhyolite is a high viscosity magma, ranging from 10^5 to 10^8 Pa s, controlled by temperature and H_2O content. In our experiments, viscosities were $10^{4.6}$ to $10^{5.2}$ Pa s

(Giordano et al, 2008; Romine and Whittington, 2015). Theoretically these viscosities should allow sufficient mobility for melt to move hundreds to thousands of microns (i.e., fill embayments) during the timescales of our experiments. Despite our manipulation of viscosity, we never achieved the ideal dense glass.

We were forced to explore new methods designed to suppress vesiculation by decreasing viscosity, increasing pressure, or allowing sintering. Examples of these approaches are briefly described herein. Synthetic core experiment CE3.1 is an example of an attempt at manipulating pressure. The capsule first dwelled at 220 MPa for 48 hours before an increase to 250 MPa for 24 hours before quench. Increasing pressure by 30 MPa should increase solubility and encourage the dissolution of bubbles. The entire embayment length was left void, meaning no melt filled the interior (Figure 3.3 panel 2, CE3.1). In another experiment focused on viscous control, pressure was held constant at 220 MPa in experiment CE4, but temperature was increased from 800 ^{o}C to 825 ^{o}C. This lowered the solubility of H_2O inconsequentially by 0.05 wt.% (Liu et al., 2005) but reduced viscosity by 40% ($10^{4.8}$ to $10^{4.6}$ Pa s). Such a significant drop should drastically improve the melt's ability to sinter and flow into the drilled embayments (Romine and Whittington, 2015). The embayment still held a bubble.

In another series of experiments, we tested the hypothesis that the problem is caused by highly viscous, rhyolite melt which cannot efficiently flow into the constricted openings of the embayments. When no material is packed into the drilled space ~30% of the synthetic embayments fill after a 96-hour dwell period, thus leaving the interior space mostly empty (Figure 3.3 panel 1, CE2). Experiment duration does not greatly change that filling amount. Next, we picked dense, glass shards roughly 50 to 100 μm in

diameter from a crushed rhyolite pumice. The shards were chosen to best fill the hole as a single piece. We manually loaded those relatively large shards into drilled embayments and capped with hydrated obsidian prior to equilibration. This approach similarly only yielded ~30% filled volume, with the remainder being void space (Figure 3.3 panel 3, CE4). Next we packed a very finely crushed powder into the drill holes. Powder most effectively fills synthetic embayments to ~60% (CE6-6.1) but results in a synthetic embayment marked by significant vesiculation and microlites.

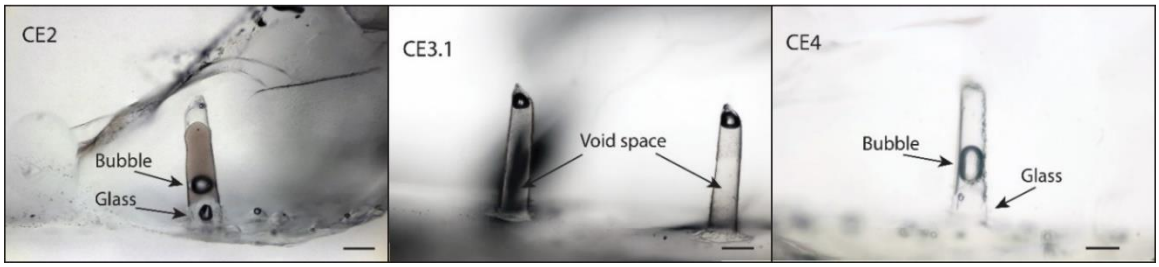

Figure 3.3. Select photomicrographs of partially filled to void synthetic embayments.

Sintering is the process of annealing glass powder. Two additional experiments were run without natural crystals or cores to test sintering timescales of our glass powder. In these sintering iterations, experiments with powder and 5 wt.% H_2O were held at 200 MPa and 800^{o}C for 2 hours before dropping the temperature to 600 ^{o}C for another 2 hours. This drop in temperature increases solubility of H_2O from 6 to 6.5 wt.%, thereby fostering resorption of bubbles introduced by fine powder and producing a dense glass (e.g., Gardner et al., 2018). For this application, the temperature would then need to be raised back to 800 ^{o}C for the actual experiment, but bubbles persisted so this was not the solution.

One possible solution is to hydrate natural embayments already filled with dense glass. I have accomplished this successfully. Hydration was successfully achieved in two

solubility experiments with natural embayments at 800 ºC and 200 MPa, and 825 ºC and 220 MPa respectively (Figure 3.4). We selected ideal, natural embayment bearing, euhedral quartz crystals and placed these inside a gold capsule with rhyolite powder and water. These were then run at temperature and pressure conditions above solubility for a minimum of 24 hours to synthetically hydrate natural embayment glass to equilibrium. These synthetically hydrated, natural embayments could then be used as starting material for decompression experiments. This approach may be the best experimental avenue going forward. At the writing and submission of the thesis I have not perfected the method to fully eliminate unwanted vesiculation. Experiments will be ongoing in the summer of 2021 as I seek to solve this problem.

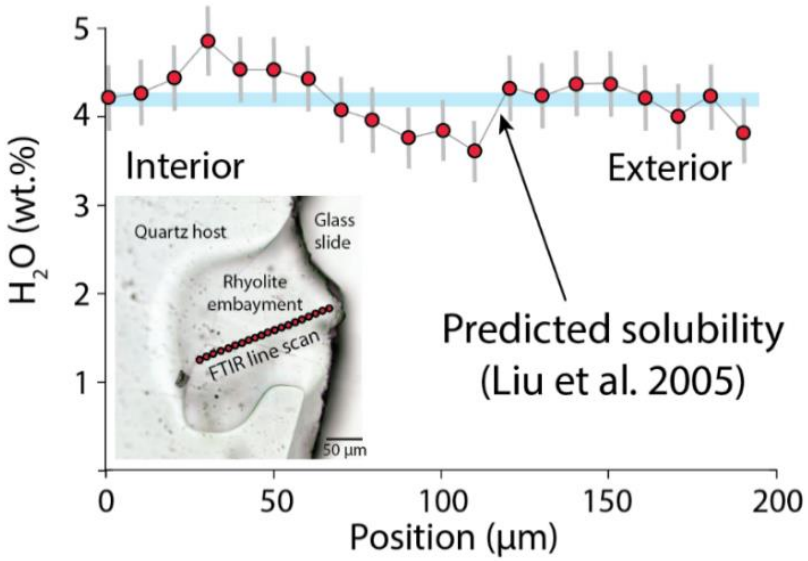

Figure 3.4. Diffusion profile from a natural, experimentally hydrated embayment from the Bishop Tuff. The retrieved flat, profile matches with predicted solubility at run conditions.

Decompression Experiments

To test my ability to run controlled decompressions, I ran 6 experiments using collections of natural quartz-hosted embayments and shallow drilled embayments. These experiments were decompressed at rates of 0.001 to 0.006 MPa s^{-1}. Nearly all embayments vesiculated and crystallized microlites (Figure 3.5). The number of natural embayments in a single experiment which vesiculated typically ranged between 80% and 100% This vesiculation blocks diffusion from operating according to theory.

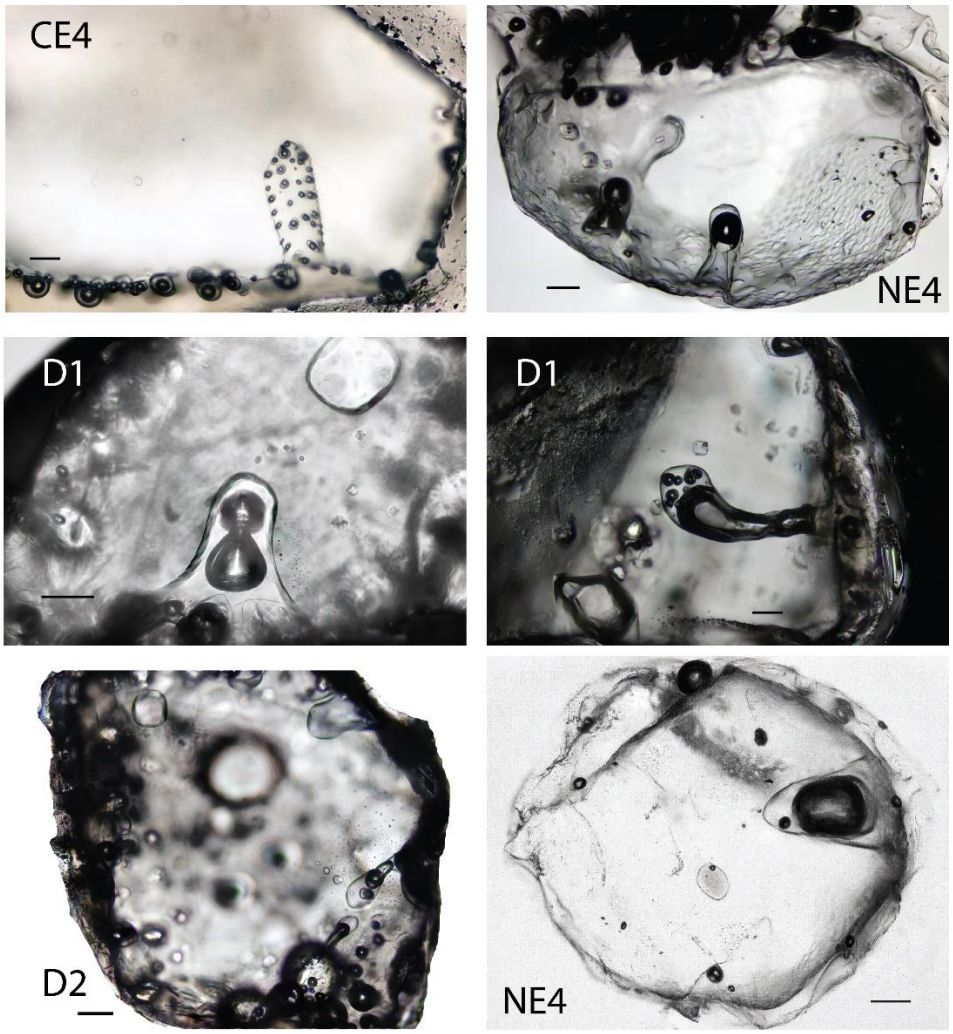

Figure 3.5. Select images of vesiculated experimentally decompressed (D1-2, NE4) and re-equilibrated (CE4) natural embayments. Refer back to Table 3.1 for experimental conditions.

Bubbles act as sinks for H_2O, creating localized concentration gradients. This deflects diffusion in a complex manner, deviating from typical 1-D models. As a result, water concentration gradients retrieved from these embayments (experiments R3 and D3) do not follow diffusion (Figure 3.6). FTIR analyses were taken in bubble-free windows of glass and the resulting profiles are not consistent with diffusion modeling, instead maintaining ~3 wt. % H_2O from the embayment interior to its exit at the mouth. Of the few glassy, natural embayments, none survived the sample preparation process to be analyzed for H_2O.

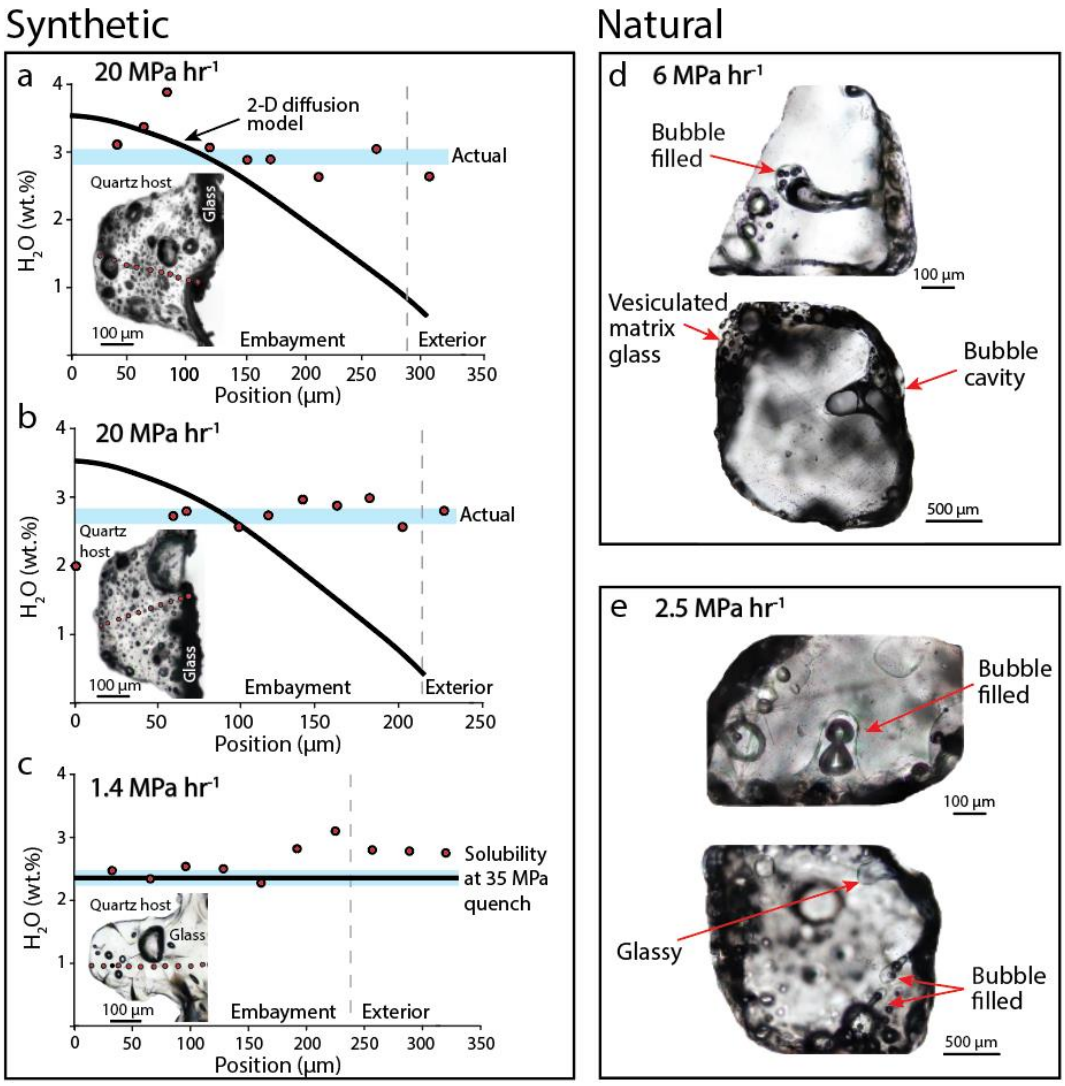

Figure 3.6. a-c) Diffusion profiles from 3 synthetic embayment decompression experiments; d-e) experimentally decompressed natural embayments showing varying degrees of vesiculation.

The vesicles and microlites produced during experiments provide another opportunity to assess the reliability of decompression rate recorded within embayments. Microlites and vesicles grow in response to decompression (Toramaru et al., 2008; Gardner, 2007; Toramaru, 2006). Bubble and microlite number density of both textures can be compared to predictions from models. I counted the number of microlites and bubbles within set volumes of glass using a petrographic microscope. Two embayments

decompressed at 20 MPa hr^{-1} are highly vesiculated, with an average bubble number density (BND) of $10^{14.8}$ m^{-3}. Microlite number density (MND) in the two embayments run at 20 MPa hr^{-1} average to $10^{4.9}$ mm^{-3} (Figure 3.7), and the single embayment at 1.4 MPa hr^{-1} yields an MND of $10^{4.3}$ mm^{-3} (Toramaru et al., 2008). These results match past MND experimental calibration and align with estimates for decompression rate. It is worth noting that these three synthetic embayments were very shallow with respect to their diameter and are poorly representative of natural embayment geometries. Embayments vesiculate differently that melt in the conduit and microlites are extremely rare. Thus, these results illustrate that experimental melt successfully records imposed decompression rates.

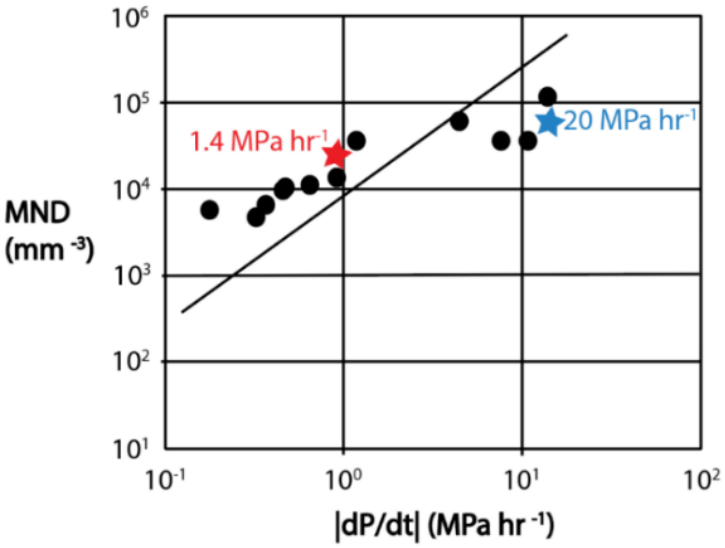

Figure 3.7. Microlite number density results from synthetic embayments plotted against decompression rate. Black circles are data from Toramaru et al., (2008), whereas our data is shown as starts.

The bubble and microlite approach is not applicable to natural embayments. We speculate that viscous shielding blocks textural maturation in natural embayments.

Viscous shielding was not effective in our experiments, allowing a good match with MND models.

Dense, glassy embayments are typically the most common filling texture across quartz-hosted embayments from explosive rhyolitic eruptions. The average relative abundance of glassy quartz-hosted embayments is 44%, whereas experiments yield <20%. This discrepancy is therefore likely imposed by experimental materials or conditions rather than natural variability. Interstitial space in between unconsolidated powder in experimental capsules likely contributes to some of this vesiculation. Microlites in powder may also provide additional bubble nucleation sites in the melt. Further experimentation with sintering of powder and the use of microlite-free powder may address these issues.

CHAPTER FOUR

Concluding Remarks

In conclusion, I will revisit the significant contributions of this work to the igneous petrology and volcanology community. First, I worked to establish a more comprehensive understanding of the occurrence, abundance, morphology, formation, and filling characteristics of quartz-hosted embayments. I conducted a descriptive and statistical survey of ten, large-volume, rhyolitic eruptions spanning geologic history and geography. I found that the abundance of embayments in quartz varies widely across different eruptive systems, potentially recording differences in magmatic storage conditions. Furthermore, glassy embayments are indeed representative of the dominant texture in embayments, but bubble textures are common and pervasive. Embayment morphology does not vary across eruptions, indicating that the mechanism controlling their formation is consistent in rhyolites. I compared natural, bubbly embayments to models which predict melt loss from embayments of various geometries and ascent rates. Ultimately, this textural and numerical analysis reveals three potential timescales for embayments: embayment diffusion speedometry, embayment emptying, and embayment faceting.

I also worked to develop an experimental approach to validate embayment speedometry. It was my hope to run a series of decompression experiments with drilled cores to test this method in a simple and controlled geometry with a complementary natural dataset. I encountered many roadblocks and challenges in this research. First, I

made many attempts to drill synthetic embayments of uniform shape and size into quartz using fine, diamond-tipped drill bits in a microdrill. This was time consuming, expensive, and ineffective, typically resulting in broken drill bits. An unforeseen opportunity in this challenge was the opportunity to think creatively and collaborate with materials scientists. Ultimately, these collaborators completed a challenging technical task and successfully produced the synthetic embayments. Most problematic, however, was the challenge of filling these synthetic embayments with clear, dense glass, suitable for FTIR analyses. Despite many experimental iterations, I was unsuccessful at the time of writing this thesis. It was, however, an invaluable exercise in developing an experimental approach, adjusting methods iteratively based on theory in response to unexpected complications. Further work to fill synthetic embayments with clear glass, or alternatively, a more brute force approach using numerous, small suites of decompressed natural embayments may yet achieve the results I sought.

Embayments are complex, small-scale recorders of large-scale, rapid magmatic and eruptive processes. Much remains unclear about their formation and ability to record these processes, yet the results presented here indicate that they do indeed capture meaningful insights into these critical timescales. This work ought to encourage and spur on the volcanological community to continue refining diffusion models and tackling an experimental assessment. These are worthwhile efforts towards further establishing embayment speedometry as a robust method to reconstruct eruptive histories.

I learned many techniques over the course of my Master's research. I used an observational, brute force approach with huge statistical numbers. Additionally, I learned how to operate an experimental lab and instruments including an FTIR, Raman, SEM,

and TEM (Figure 4.1). These tools will provide an analytical platform to propel me into the next step in my career. This work has fueled my fascination and excitement for magmatic and volcanic processes and their crystalline recorders. During my Ph.D. at Stanford University, I will focus this enthusiasm towards unravelling the processes which allow for and inhibit the generation and eruption of large volume, explosive silicic bodies.

Figure 4.1. Removing and quenching an experiment in the high-pressure high-temperature lab at Baylor.

Figure 4.1. Providing a scale for the Yellowstone, Huckleberry Ridge Tuff fall deposit at the Mount Everts exposure.

APPENDIX

APPENDIX

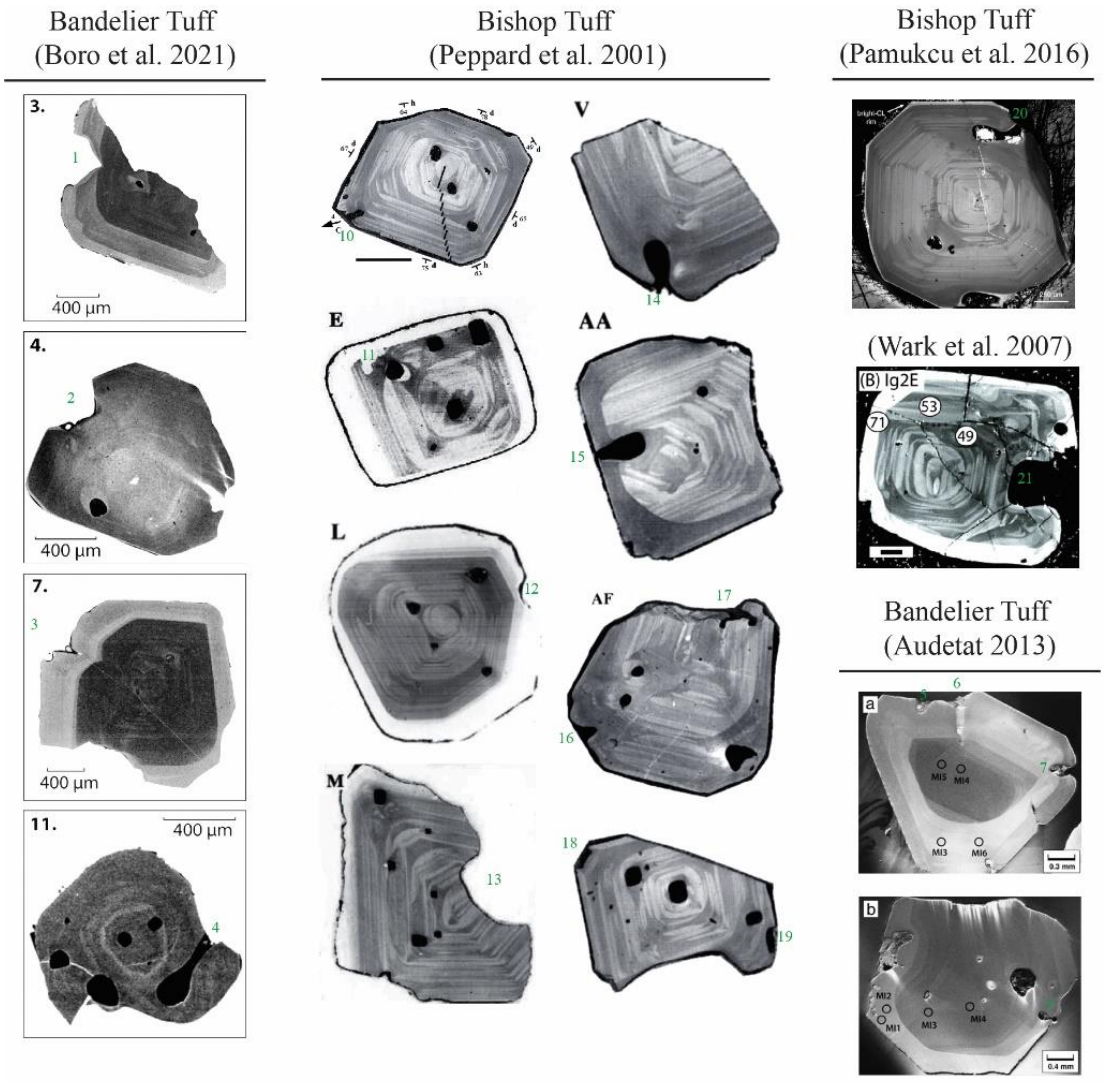

Figure A.1. Quartz CL imagery literature compilation panel 1.

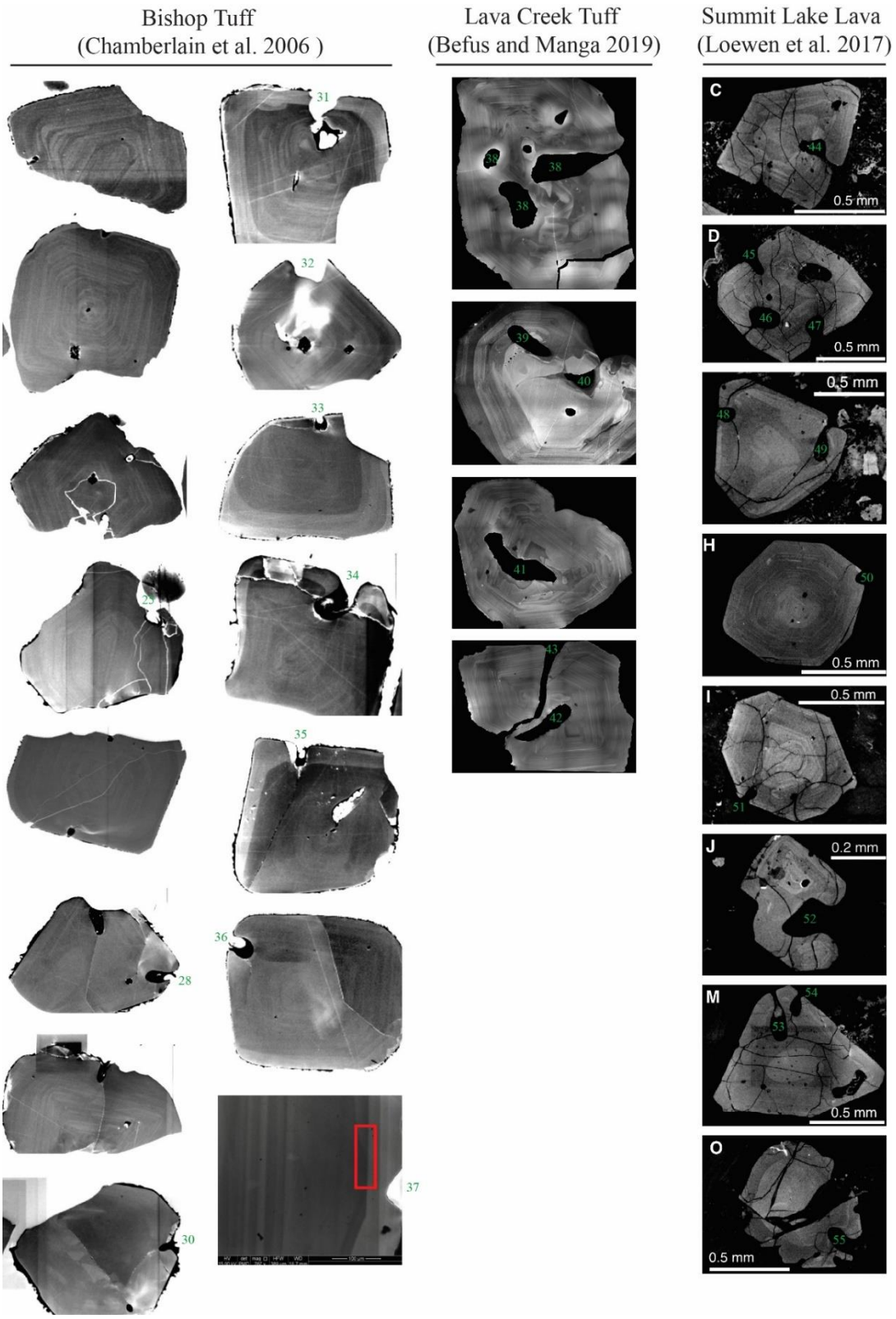

Figure A.2. Quartz CL imagery literature compilation panel 2.

Figure A.3. Quartz CL imagery literature compilation panel 3.

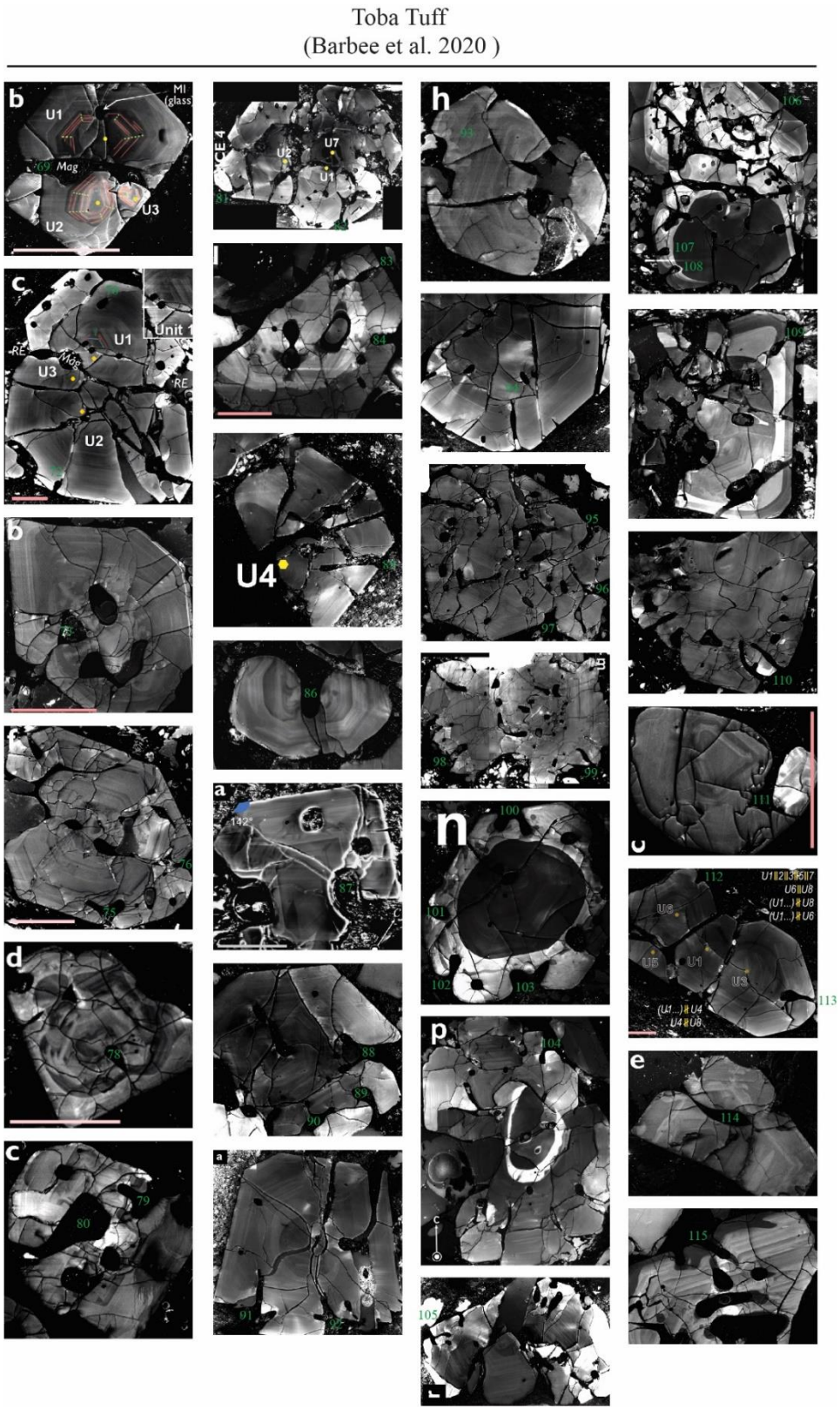

Figure A.4. Quartz CL imagery literature compilation panel 4.

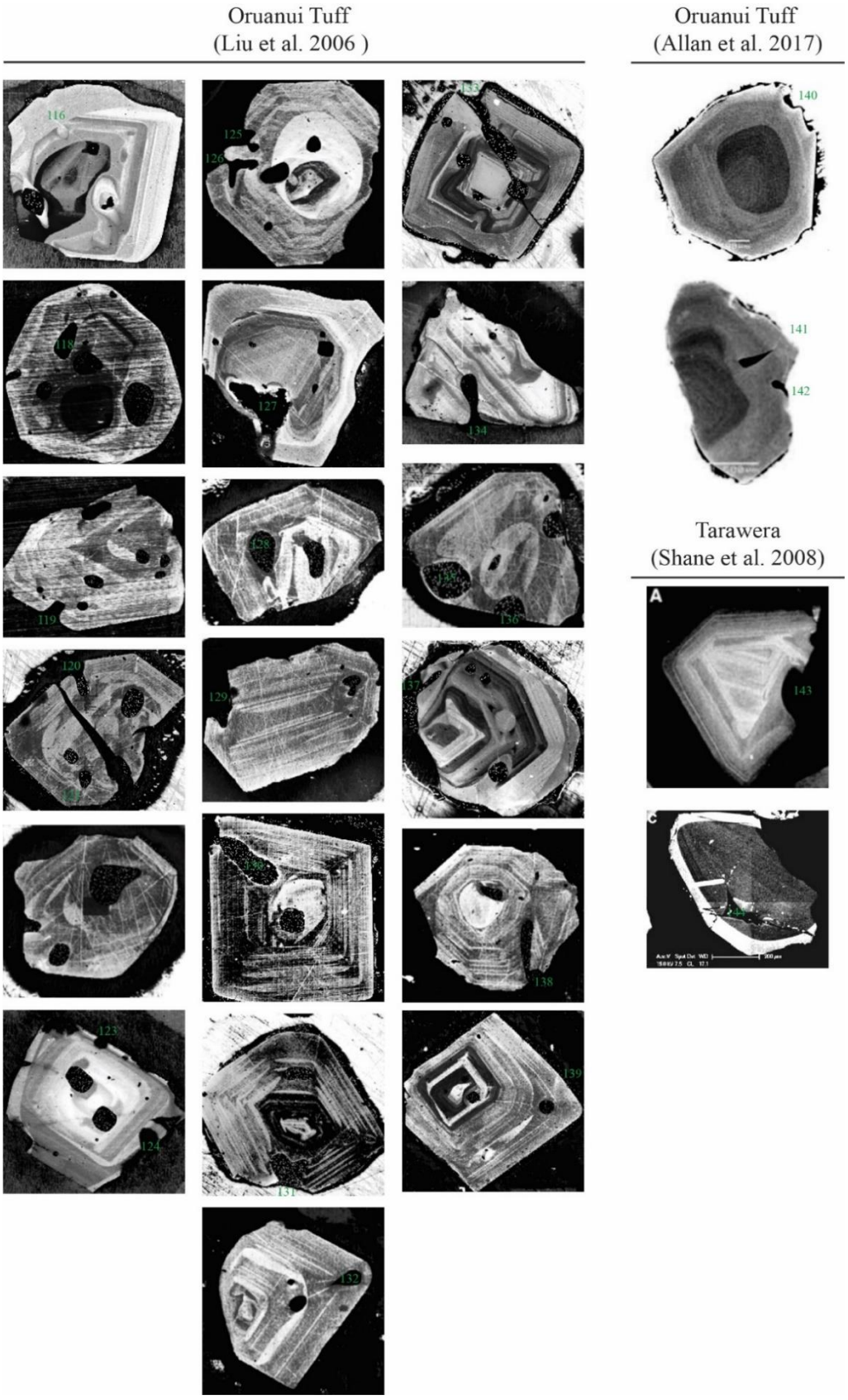

Figure A.5. Quartz CL imagery literature compilation panel 5.

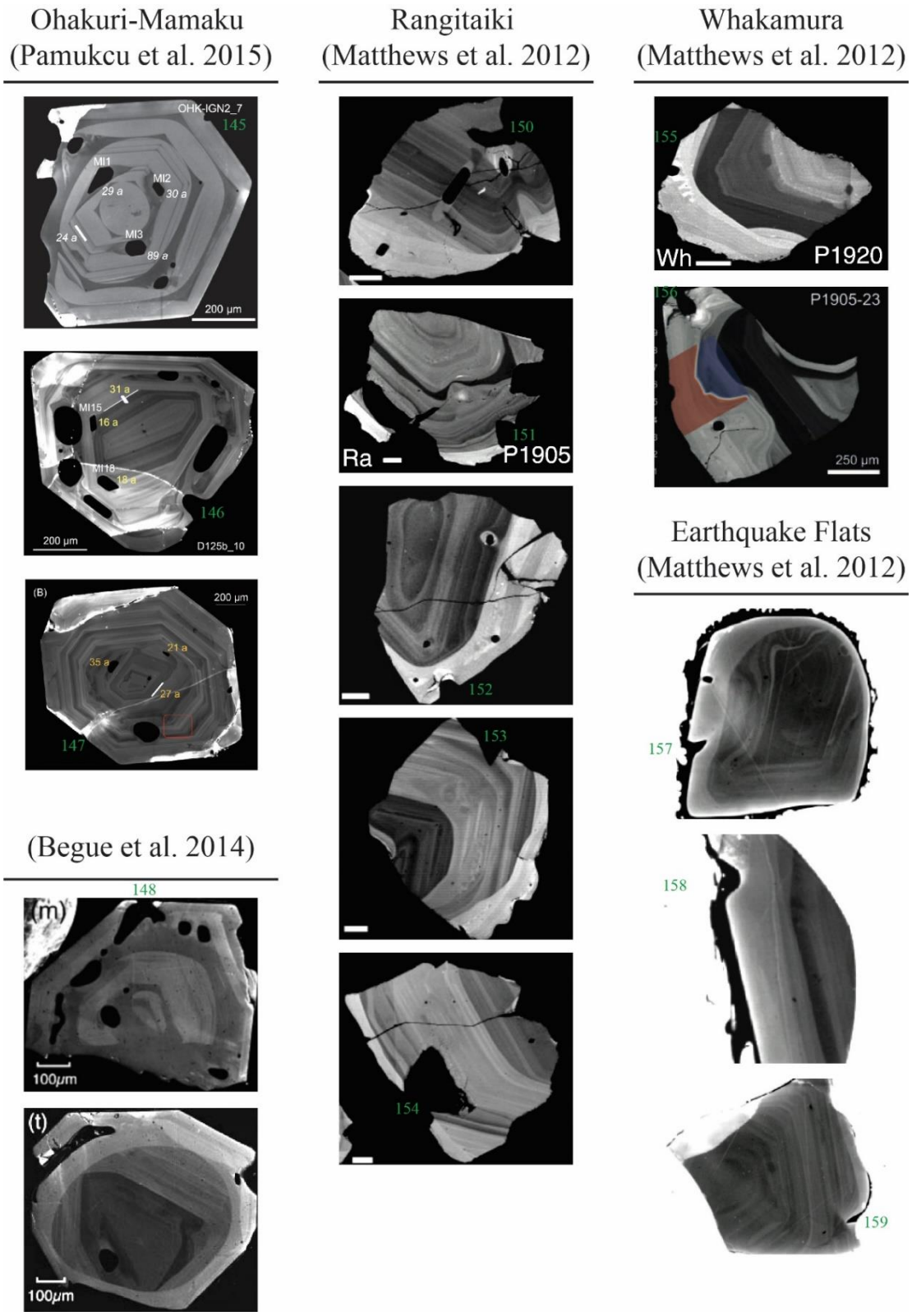

Figure A.6. Quartz CL imagery literature compilation panel 6.

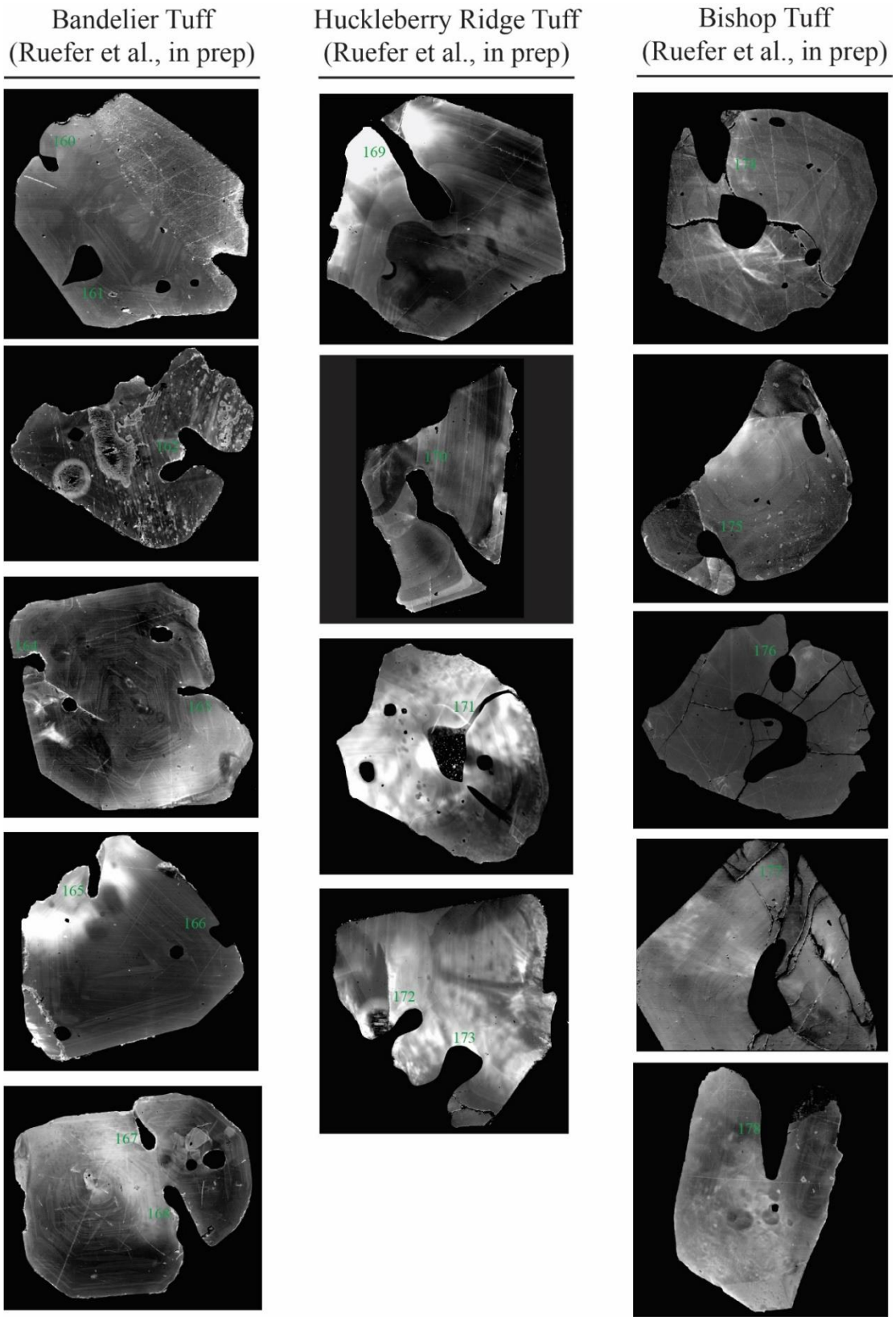

Figure A.7. Quartz CL imagery compilation from this study panel 7.

REFERENCES

Allan, A. S., Barker, S. J., Millet, M. A., Morgan, D. J., Rooyakkers, S. M., Schipper, C. I., and Wilson, C. J. (2017). A cascade of magmatic events during the assembly and eruption of a super-sized magma body. Contrib. Mineral. Petrol., 172(7), 1-34. doi.org/10.1007/s00410-017-1367-8

Allison, C. M., Roggensack, K., & Clarke, A. B. (2021). Highly explosive basaltic eruptions driven by CO 2 exsolution. Nature communications, 12(1), 1-10.

Anderson, A. T. (1991). Hourglass inclusions: Theory and application to the Bishop Rhyolitic Tuff. 18.

Anderson, A. T., 2006, Bubbleless glass pockets and natural bubble nucleation in rhyolitic magma: EOS Trans, AGU, 87, Fall Meeting Suppl., Abstract V43A-1785.

Andrews, B. J., & Befus, K. S. (2020). Supersaturation nucleation and growth of plagioclase: a numerical model of decompression-induced crystallization. Contributions to Mineralogy and Petrology, 175(3), 1-20.

Audétat, A. (2013). Origin of Ti-rich rims in quartz phenocrysts from the Upper Bandelier Tuff and the Tunnel Spring Tuff, southwestern USA. Chem. Geol., 360, 99-104. doi.org/10.1016/j.chemgeo.2013.10.015.

Barbee, O., Chesner, C., & Deering, C. (2020). Quartz crystals in Toba rhyolites show textures symptomatic of rapid crystallization. American Mineralogist: Journal of Earth and Planetary Materials, 105(2), 194-226.

Befus, K. S., and Manga, M. (2019). Supereruption quartz crystals and the hollow reentrants. Geology 47, 710–714. doi:10.1130/G46275.1.

Befus, K. S., and Andrews, B. J. (2018). Crystal nucleation and growth produced by continuous decompression of Pinatubo magma. Contrib. Mineral. Petrol., 173(11), 1-20. doi.org/10.1007/s00410-018-1519-5.

Bégué, F., Deering, C. D., Gravley, D. M., Kennedy, B. M., Chambefort, I., Gualda, G. A., and Bachmann, O. (2014). Extraction, storage and eruption of multiple isolated magma batches in the paired Mamaku and Ohakuri eruption, Taupo Volcanic Zone, New Zealand. J. Petrol., 55(8), 1653-1684. doi.org/10.1093/petrology/egu038

Boro, J. R., Wolff, J. A., Neill, O. K., Steiner, A. R., and Ramos, F. C. (2021). Titanium diffusion profiles and melt inclusion chemistry and morphology in quartz from the Tshirege Member of the Bandelier Tuff. Am Min.,106(4), 620-632. doi.org/10.2138/am-2021-7395.

Browne, B. L., & Gardner, J. E. (2006). The influence of magma ascent path on the texture, mineralogy, and formation of hornblende reaction rims. Earth and Planetary Science Letters, 246(3-4), 161-176.

Busby, T. S., & Barker, J. (1966). Simulative studies of upward drilling. Journal of the American Ceramic Society, 49(8), 441-446.

Cashman, K. V. (1992). Groundmass crystallization of Mount St. Helens dacite, 1980?1986: a tool for interpreting shallow magmatic processes. Contrib. Mineral. Petrol. 109, 431–449. doi:10.1007/BF00306547.

Cassidy, M. (2018). Controls on explosive-effusive volcanic eruption styles. Nature Communications, 16.

Castro, J. M., and Dingwell, D. B. (2009). Rapid ascent of rhyolitic magma at Chaitén volcano, Chile. Nature 461, 780–783. doi:10.1038/nature08458.

Castro, J. M., and Gardner, J. E. (2008). Did magma ascent rate control the explosive-effusive transition at the Inyo volcanic chain, California. Geology 36, 279. doi:10.1130/G24453A.1.

Chamberlain, K. J., Morgan, D. J., and Wilson, C. J. (2014). Timescales of mixing and mobilization in the Bishop Tuff magma body: perspectives from diffusion chronometry. Contrib. Mineral. Petrol., 168(1), 1034. doi.org/10.1007/s00410-014-1034-2.

Coumans, J. P., Llewellin, E. W., Humphreys, M. C., Nowak, M., Brooker, R. A., Mathias, S. A., & McIntosh, I. M. (2020). An experimentally-validated numerical model of diffusion and speciation of water in rhyolitic silicate melt. Geochimica et Cosmochimica Acta, 276, 219-238.

deGraffenried, R. L., & Shea, T. (2021). Using Volatile Element Concentration Profiles in Crystal-Hosted Melt Embayments to Estimate Magma Decompression Rate: Assumptions and Inherited Errors. Geochemistry, Geophysics, Geosystems, 22(5), e2021GC009672.

Donaldson, C. H., & Henderson, C. M. B. (1988). A new interpretation of round embayments in quartz crystals. Mineralogical Magazine, 52(364), 27-33.

Ferguson, D. J., Gonnermann, H. M., Ruprecht, P., Plank, T., Hauri, E. H., Houghton, B. F., et al. (2016). Magma decompression rates during explosive eruptions of Kīlauea volcano, Hawaii, recorded by melt embayments. Bull. Volcanol. 78, 71. doi:10.1007/s00445-016-1064-x.

Frezzotti, M. L. (2001). Silicate-melt inclusions in magmatic rocks: applications to petrology. Lithos, 55(1-4), 273-299.

Gardner, J. E., Hilton, M., & Carroll, M. R. (2000). Bubble growth in highly viscous silicate melts during continuous decompression from high pressure. Geochimica et Cosmochimica Acta, 64(8), 1473-1483.

Gardner, J. E., Llewellin, E. W., Watkins, J. M., and Befus, K. S. (2017). Formation of obsidian pyroclasts by sintering of ash particles in the volcanic conduit. Earth Planet. Sci. Lett. 459, 252–263. doi:10.1016/j.epsl.2016.11.037.

Gardner, J. E. (2007). Heterogeneous bubble nucleation in highly viscous silicate melts during instantaneous decompression from high pressure. Chem.Geol., 236(1-2), 1-12. doi.org/10.1016/j.chemgeo.2006.08.006.

Giordano, D., Russell, J. K., and Dingwell, D. B. (2008). Viscosity of magmatic liquids: a model. Earth Planet. Sci. Lett., 271(1-4), 123-134. doi.org/10.1016/j.epsl.2008.03.038.

Gonnermann, H. M., & Manga, M. (2007). The fluid mechanics inside a volcano. Annu. Rev. Fluid Mech., 39, 321-356.

Gualda, G. A., & Anderson, A. T. (2007). Magnetite scavenging and the buoyancy of bubbles in magmas. Part 1: Discovery of a pre-eruptive bubble in Bishop rhyolite. Contributions to Mineralogy and Petrology, 153(6), 733-742.

Gualda, G. A., Pamukcu, A. S., Ghiorso, M. S., Anderson Jr, A. T., Sutton, S. R., & Rivers, M. L. (2012). Timescales of quartz crystallization and the longevity of the Bishop giant magma body. PloS one, 7(5), e37492.

Hajimirza, S., Gonnermann, H. M., and Gardner, J. E. (2021). Reconciling bubble nucleation in explosive eruptions with geospeedometers. Nature Communications 12, 283. doi:10.1038/s41467-020-20541-1.

Hamada, M., Laporte, D., Cluzel, N., Koga, K. T., and Kawamoto, T. (2010). Simulating bubble number density of rhyolitic pumices from Plinian eruptions: constraints from fast decompression experiments. Bull.Volcanol., 72(6), 735-746. doi.org/10.1007/s00445-010-0353-z.

Harris, D. M., & Anderson, A. T. (1984). Volatiles H 2 O, CO 2, and Cl in a subduction related basalt. Contributions to Mineralogy and Petrology, 87(2), 120-128.

Hervig, R. L., & Dunbar, N. W. (1992). Cause of chemical zoning in the Bishop (California) and Bandelier (New Mexico) magma chambers. Earth and Planetary Science Letters, 111(1), 97-108.

Humphreys, M. C. S., Menand, T., Blundy, J. D., and Klimm, K. (2008). Magma ascent rates in explosive eruptions: Constraints from H2O diffusion in melt inclusions. Earth Planet. Sci. Lett. 270, 25–40. doi:10.1016/j.epsl.2008.02.041.

Hurwitz, S., & Navon, O. (1994). Bubble nucleation in rhyolitic melts: Experiments at high pressure, temperature, and water content. Earth and Planetary Science Letters, 122(3-4), 267-280.

Cashman, K. V. (2004). Volatile controls on magma ascent and eruption. The State of the Planet: Frontiers and Challenges in Geophysics, 150, 109-124.

Lemmlein, (1930). Corrosion and regeneration of quartz phenocrysts in quartz porphyries. Doklady Akad. Nauk SSSR A-3, 341-344.

Liu, Y., Anderson, A. T., and Wilson, C. J. N. (2007). Melt pockets in phenocrysts and decompression rates of silicic magmas before fragmentation. J. Geophys. Res. 112, B06204. doi:10.1029/2006JB004500.

Liu, Y., Anderson, A. T., Wilson, C. J., Davis, A. M., and Steele, I. M. (2006). Mixing and differentiation in the Oruanui rhyolitic magma, Taupo, New Zealand: evidence from volatiles and trace elements in melt inclusions. Contrib. Mineral. Petrol., 151(1), 71-87. doi.org/10.1007/s00410-005-0046-3.

Liu, Y., Zhang, Y., and Behrens, H. (2005). Solubility of H_2O in rhyolitic melts at low pressures and a new empirical model for mixed H_2O–CO_2 solubility in rhyolitic melts. J. Volcanol. Geotherm. Res., 143(1-3), 219-235. doi.org/10.1016/j.jvolgeores.2004.09.019.

Lloyd, A. S., Ruprecht, P., Hauri, E. H., Rose, W., Gonnermann, H. M., and Plank, T. (2014). NanoSIMS results from olivine-hosted melt embayments: Magma ascent rate during explosive basaltic eruptions. J. Volcanol. Geotherm. Res. 283, 1–18. doi:10.1016/j.jvolgeores.2014.06.002.

Loewen, M. W., Bindeman, I. N., & Melnik, O. E. (2017). Eruption mechanisms and short duration of large rhyolitic lava flows of Yellowstone. Earth Planet. Sci. Lett., 458, 80-91. doi.org/10.1016/j.epsl.2016.10.034.

Lowenstern, J. B. (2003). “Melt inclusions come of age: Volatiles, volcanoes, and sorby’s legacy,” in Developments in Volcanology (Elsevier), 1–21. doi:10.1016/S1871-644X(03)80021-9.

Lowenstern, J. B., & Thompson, J. F. H. (1995). Applications of silicate-melt inclusions to the study of magmatic volatiles. Magmas, fluids and ore deposits, 23, 71-99.

Mangan, M., & Sisson, T. (2000). Delayed, disequilibrium degassing in rhyolite magma: decompression experiments and implications for explosive volcanism. Earth and Planetary Science Letters, 183(3-4), 441-455.

Mastin, L. G. (2002). Insights into volcanic conduit flow from an open-source numerical model. Geochemistry, Geophysics, Geosystems, 3(7), 1-18.

Matthews, N. E., Huber, C., Pyle, D. M., & Smith, V. C. (2012). Timescales of magma recharge and reactivation of large silicic systems from Ti diffusion in quartz. J Petrol., 53(7), 1385-1416. doi.org/10.1093/petrology/egs020.

McCanta, M. C., Rutherford, M. J., and Hammer, J. E. (2007). Pre-eruptive and syn-eruptive conditions in the Black Butte, California dacite: Insight into crystallization kinetics in a silicic magma system. J. Volcanol. Geotherm. Res., 160(3-4), 263-284. doi.org/10.1016/j.jvolgeores.2006.10.004.

Moussallam, Y., Rose-Koga, E. F., Koga, K. T., Médard, E., Bani, P., Devidal, J.-L., et al. (2019). Fast ascent rate during the 2017–2018 Plinian eruption of Ambae (Aoba) volcano: a petrological investigation. Contrib. Mineral. Petrol. 174, 90. doi:10.1007/s00410-019-1625-z.

Müller, A., Breiter, K., Seltmann, R., and Pécskay, Z. (2005). Quartz and feldspar zoning in the eastern Erzgebirge volcano-plutonic complex (Germany, Czech Republic): evidence of multiple magma mixing. Lithos, 80(1-4), 201-227. doi.org/10.1016/j.lithos.2004.05.011

Myers, M. L., Druitt, T. H., Schiavi, F., Gurioli, L., and Flaherty, T. (2021). Evolution of magma decompression and discharge during a Plinian event (Late Bronze-Age eruption, Santorini) from multiple eruption-intensity proxies. Bull. Volcanol. 83, 18. doi:10.1007/s00445-021-01438-3.

Myers, M. L., Wallace, P. J., Wilson, C. J. N., Morter, B. K., and Swallow, E. J. (2016). Prolonged ascent and episodic venting of discrete magma batches at the onset of the Huckleberry Ridge supereruption, Yellowstone. Earth Planet. Sci. Lett. 451, 285–297. doi:10.1016/j.epsl.2016.07.023.

Myers, M. L., Wallace, P. J., Wilson, C. J. N., Watkins, J. M., and Liu, Y. (2018). Ascent rates of rhyolitic magma at the onset of three caldera-forming eruptions. Am. Mineral. 103, 952–965. doi:10.2138/am-2018-6225.

Nakada, S., & Motomura, Y. (1999). Petrology of the 1991–1995 eruption at Unzen: effusion pulsation and groundmass crystallization. Journal of Volcanology and Geothermal Research, 89(1-4), 173-196.

Newcombe, M. E., Plank, T., Barth, A., Asimow, P. D., and Hauri, E. (2020). Water-in-olivine magma ascent chronometry: Every crystal is a clock. J. Volcanol. Geotherm. Res. 398, 106872. doi:10.1016/j.jvolgeores.2020.106872.

Newman, S., Stolper, E. M., & Epstein, S. (1986). Measurement of water in rhyolitic glasses; calibration of an infrared spectroscopic technique. American Mineralogist, 71(11-12), 1527-1541.

Ni, H., & Zhang, Y. (2008). H2O diffusion models in rhyolitic melt with new high pressure data. Chemical Geology, 250(1-4), 68-78.

Nowak, M., & Behrens, H. (1997). An experimental investigation on diffusion of water in haplogranitic melts. Contributions to Mineralogy and Petrology, 126(4), 365-376.

Ohlhorst, S., Behrens, H., & Holtz, F. (2001). Compositional dependence of molar absorptivities of near-infrared OH-and H2O bands in rhyolitic to basaltic glasses. Chemical geology, 174(1-3), 5-20.

Pamukcu, A. S., Gualda, G. A. R., Bégué, F., and Gravley, D. M. (2015). Melt inclusion shapes: Timekeepers of short-lived giant magma bodies. Geology 43, 947–950. doi:10.1130/G37021.1.

Pamukcu, A. S., Ghiorso, M. S., and Gualda, G. A. (2016). High-Ti, bright-CL rims in volcanic quartz: a result of very rapid growth. Contrib. Mineral. Petrol., 171(12), 1-9. doi.org/10.1007/s00410-016-1317-x.

Peppard, B. T., Steele, I. M., Davis, A. M., Wallace, P. J., and Anderson, A. T. (2001). Zoned quartz phenocrysts from the rhyolitic Bishop Tuff. Am. Min., 86(9), 1034-1052. doi.org/10.2138/am-2001-8-910

Roedder, E. (1979). Origin and significance of magmatic inclusions. Bulletin de Mineralogie, 102(5), 487-510.

Romine, W. L., and Whittington, A. G. (2015). A simple model for the viscosity of rhyolites as a function of temperature, pressure and water content. Geochim. Cosmochim. Acta, 170, 281-300. doi.org/10.1016/j.gca.2015.08.009.

Rust, A., and Cashman, K. (2017). Interpretations of phenocryst embayments. 1.

Rutherford, M. J. (2008). Magma Ascent Rates. Rev. Mineral. Geochem. 69, 241–271. doi:10.2138/rmg.2008.69.7.

Rutherford, M. J., and Hill, P. M. (1993). Magma ascent rates from amphibole breakdown: an experimental study applied to the 1980–1986 Mount St. Helens eruptions. J.Geophys.Res.: Solid Earth, 98(B11), 19667-19685. doi.org/10.1029/93JB01613.

Shane, P., Smith, V. C., and Nairn, I. (2008). Millennial timescale resolution of rhyolite magma recharge at Tarawera volcano: insights from quartz chemistry and melt inclusions. Contrib. Mineral. Petrol., 156(3), 397-411. doi.org/10.1007/s00410-008-0292-2.

Steele-MacInnis, M., Esposito, R., Moore, L. R., & Hartley, M. E. (2017). Heterogeneously entrapped, vapor-rich melt inclusions record pre-eruptive magmatic volatile contents. Contributions to Mineralogy and Petrology, 172(4), 18.

Stolper, E. (1982). The speciation of water in silicate melts. Geochimica et Cosmochimica Acta, 46(12), 2609-2620.

Toramaru, A. (2006). BND (bubble number density) decompression rate meter for explosive volcanic eruptions. J. Volcanol. Geotherm. Res. 154, 303–316. doi:10.1016/j.jvolgeores.2006.03.027.

Toramaru, A., Noguchi, S., Oyoshihara, S., and Tsune, A. (2008). MND(microlite number density) water exsolution rate meter. J. Volcanol. Geotherm. Res. 175, 156–167. doi:10.1016/j.jvolgeores.2008.03.035.

Vazquez, J. A., Kyriazis, S. F., Reid, M. R., Sehler, R. C., and Ramos, F. C. (2009). Thermochemical evolution of young rhyolites at Yellowstone: Evidence for a cooling but periodically replenished postcaldera magma reservoir. J. Volcanol. Geotherm. Res., 188(1-3), 186-196. doi.org/10.1016/j.jvolgeores.2008.11.030.

Wark, D. A., Hildreth, W., Spear, F. S., Cherniak, D. J., and Watson, E. B. (2007). Pre-eruption recharge of the Bishop magma system. Geol., 35(3), 235-238. doi.org/10.1130/G23316A.1.

Wallace, P. J., Anderson, A. T., & Davis, A. M. (1995). Quantification of pre-eruptive exsolved gas contents in silicic magmas. Nature, 377(6550), 612-616.

Waters, L. E., Andrews, B. J., and Lange, R. A. (2015). Rapid crystallization of plagioclase phenocrysts in silicic melts during fluid-saturated ascent: phase equilibrium and decompression experiments. J. Petrol., 56(5), 981-1006. doi.org/10.1093/petrology/egv025.

Watkins, J. M., Manga, M., & DePaolo, D. J. (2012). Bubble geobarometry: A record of pressure changes, degassing, and regassing at Mono Craters, California. Geology, 40(8), 699-702.

Wilson, L. (1980). Relationships between pressure, volatile content and ejecta velocity in three types of volcanic explosion. Journal of Volcanology and Geothermal Research, 8(2-4), 297-313.

Wilson, C. J., Blake, S., Charlier, B. L. A., & Sutton, A. N. (2006). The 26· 5 ka Oruanui eruption, Taupo volcano, New Zealand: development, characteristics and evacuation of a large rhyolitic magma body. Journal of Petrology, 47(1), 35-69.

Withers, A. C., & Behrens, H. (1999). Temperature-induced changes in the NIR spectra of hydrous albitic and rhyolitic glasses between 300 and 100 K. Physics and Chemistry of Minerals, 27(2), 119-132.

Wolf, K. J., and Eichelberger, J. C. (1997). Syneruptive mixing, degassing, and crystallization at Redoubt Volcano, eruption of December, 1989 to May 1990. J. Volcanol. Geotherm. Res., 75(1-2), 19-37.

Zhang, Y. (2010). Diffusion in minerals and melts: theoretical background. Reviews in mineralogy and geochemistry, 72(1), 5-59.

Zhang, Y., Xu, Z., Zhu, M., & Wang, H. (2007). Silicate melt properties and volcanic eruptions. Reviews of Geophysics, 45(4).